Atmospheric
Measurement
Techniques

Evaluating the impact of spatial resolution on tropospheric NO$_2$ column comparisons within urban areas using high-resolution airborne data

Laura M. Judd[1,2], **Jassim A. Al-Saadi**[1], **Scott J. Janz**[3], **Matthew G. Kowalewski**[3,4], **R. Bradley Pierce**[5], **James J. Szykman**[6], **Lukas C. Valin**[6], **Robert Swap**[3], **Alexander Cede**[7], **Moritz Mueller**[7,8], **Martin Tiefengraber**[7,8], **Nader Abuhassan**[3,9], **and David Williams**[6]

[1]NASA Langley Research Center, Hampton, VA 23681, USA
[2]NASA Postdoctoral Program, Hampton, VA 23681, USA
[3]NASA Goddard Space Flight Center, Greenbelt, MD 20771, USA
[4]Universities Space Research Association, Columbia, MD 21046, USA
[5]University of Wisconsin–Madison Space Science and Engineering Center, Madison, WI 53706, USA
[6]United States Environmental Protection Agency Office of Research and Development,
Research Triangle Park, NC 27709, USA
[7]LuftBlick, Kreith, Austria
[8]Department of Atmospheric and Cryospheric Science, University of Innsbruck, Innsbruck, Austria
[9]Joint Center for Earth Systems Technology, University of Maryland, Baltimore County, Baltimore, MD 21228, USA

Correspondence: Laura M. Judd (laura.m.judd@nasa.gov)

Abstract. NASA deployed the GeoTASO airborne UV–visible spectrometer in May–June 2017 to produce high-resolution (approximately 250 m × 250 m) gapless NO$_2$ datasets over the western shore of Lake Michigan and over the Los Angeles Basin. The results collected show that the airborne tropospheric vertical column retrievals compare well with ground-based Pandora spectrometer column NO$_2$ observations ($r^2 = 0.91$ and slope of 1.03). Apparent disagreements between the two measurements can be sensitive to the coincidence criteria and are often associated with large local variability, including rapid temporal changes and spatial heterogeneity that may be observed differently by the sunward-viewing Pandora observations. The gapless mapping strategy executed during the 2017 GeoTASO flights provides data suitable for averaging to coarser areal resolutions to simulate satellite retrievals. As simulated satellite pixel area increases to values typical of TEMPO (Tropospheric Emissions: Monitoring Pollution), TROPOMI (TROPOspheric Monitoring Instrument), and OMI (Ozone Monitoring Instrument), the agreement with Pandora measurements degraded, particularly for the most polluted columns

as localized large pollution enhancements observed by Pandora and GeoTASO are spatially averaged with nearby less-polluted locations within the larger area representative of the satellite spatial resolutions (aircraft-to-Pandora slope: TEMPO scale = 0.88; TROPOMI scale = 0.77; OMI scale = 0.57). In these two regions, Pandora and TEMPO or TROPOMI have the potential to compare well at least up to pollution scales of 30×10^{15} molecules cm^{-2}. Two publicly available OMI tropospheric NO$_2$ retrievals are found to be biased low with respect to these Pandora observations. However, the agreement improves when higher-resolution a priori inputs are used for the tropospheric air mass factor calculation (NASA V3 standard product slope = 0.18 and Berkeley High Resolution product slope = 0.30). Overall, this work explores best practices for satellite validation strategies with Pandora direct-sun observations by showing the sensitivity to product spatial resolution and demonstrating how the high-spatial-resolution NO$_2$ data retrieved from airborne spectrometers, such as GeoTASO, can be used with high-temporal-resolution ground-based column observations

to evaluate the influence of spatial heterogeneity on validation results.

1 Introduction

Nitrogen oxides (NO$_x$: NO + NO$_2$) are primarily emitted via fossil fuel combustion, soil microbial processes, biomass burning, and lightning. NO$_2$ is an important precursor of ozone and particulate matter, making it one of the six criteria air pollutants monitored by the United States Environmental Protection Agency (EPA: https://www.epa.gov/criteria-air-pollutants, last access: 31 October 2019). Unlike less reactive trace gases having atmospheric lifetimes of days or longer, the atmospheric lifetime of NO$_x$ is reported to be on the order of hours in the daytime polluted boundary layer (Liang et al., 1998; Beirle et al., 2011; Liu et al., 2016). This short lifetime along with large variations in emission rates from sources causes the spatial distribution of NO$_2$ in polluted regions to be highly heterogeneous, making it difficult to characterize over urban areas without high spatiotemporal observations.

Since the 1990s, NO$_2$ column densities have been monitored globally from sun-synchronous satellite platforms utilizing the differential optical absorption spectroscopy (DOAS) methodology applied to earthshine spectra in the visible-blue wavelengths. The nadir spatial resolution of these sensors has generally improved over time – beginning with the Global Ozone Monitoring Experiment (GOME) at 40 km × 320 km in 1995 (Burrows et al., 1999), dramatically refining a decade later with the Ozone Monitoring Instrument (OMI) at 13 km × 24 km in 2004 (Levelt et al., 2006), and improving most recently to a subcity spatial scale from the TROPOspheric Monitoring Instrument (TROPOMI) instrument aboard Sentinel-5P launched October 2017 with a nadir spatial resolution of 3.5 km × 7 km (van Geffen et al., 2019).

OMI has been a prominent resource for understanding the global distribution of tropospheric NO$_2$ since its launch. However, shortfalls have been documented regarding its inability to capture the spatial variability within polluted regions (e.g., Valin et al., 2011a, b; Broccardo et al., 2018). This inability is further hindered by the use of coarse a priori assumptions in the air mass factor (AMF) calculation for slant-to-vertical column conversion (Heckel et al., 2011; Russell et al., 2011; Goldberg et al., 2017). Though TROPOMI observes NO$_2$ at a spatial resolution an order of magnitude finer than OMI, its sun-synchronous orbit still limits lower- to midlatitude observations to the early afternoon hours. However, within the next decade three geostationary air quality monitoring missions will be launched that will be able to monitor daytime air quality hourly at spatial scales of less than 10 km. These missions include observations of North America with Tropospheric Emissions: Monitoring Pollution (TEMPO) (Zoogman et al., 2017), Asia

with the Geostationary Environment Monitoring Spectrometer (GEMS) (Kim et al., 2017), and Europe with the Sentinel-4/Ultraviolet/Visible/Near-Infrared Instrument (UVN) (Ingmann et al., 2012). These geostationary measurements over industrialized regions of the Northern Hemisphere along with ongoing global daily sun-synchronous measurements will be important contributors to the goal of creating an atmospheric composition global observing network (IGACO, 2004; CEOS, 2011).

To prepare for these planned geostationary air quality missions, NASA supported the development of airborne ultraviolet–visible (UV–VIS) mapping instruments (Geostationary Trace Gas and Aerosol Sensor Optimization: GeoTASO, and GEO-CAPE Airborne Simulator: GCAS) to help determine the satellite instrument requirements for measurements relevant to air quality and to facilitate retrieval algorithm development at fine spatial resolutions at all times of day (Leitch et al., 2014; Kowalewski and Janz, 2014; Nowlan et al., 2016, 2018; Lamsal et al., 2017). These instruments have the capability of retrieving NO$_2$ at subkilometer spatial resolutions which can be useful in assessing trace gas heterogeneity at spatial scales finer than those of current and planned space-based retrievals. Similar instruments have also been developed by other countries. In the last decade, airborne spectrometers have mapped high-resolution NO$_2$ in parts of Europe (Popp et al., 2012; Schönhardt et al 2015; Lawrence et al., 2015; Meier et al., 2017; Tack et al., 2017, 2019), the United States (Nowlan et al., 2016, 2018; Lamsal et al., 2017; Judd et al., 2018), Asia (Judd et al., 2018), and Africa (Broccardo et al., 2018). Results from these efforts have illustrated the capability of airborne spectrometers to observe the impact of emission sources and meteorology on the spatial distribution of NO$_2$ (Popp et al., 2012; Schönhardt et al., 2015; Judd et al., 2018, and Tack et al., 2019) and have shown utility for evaluating NO$_x$ emissions (Schönhardt et al., 2015; Souri et al., 2018) as these high-resolution measurements can resolve detailed NO$_2$ spatial patterns that satellites, at their current spatial resolutions, cannot (Broccardo et al., 2018; Lamsal et al., 2017; Judd et al., 2018).

Measurements from these airborne UV–VIS mapping instruments can provide a transfer standard between the space-based sensor footprint and ground-based column measurements used for validation of the satellite trace gas products, such as NO$_2$ tropospheric vertical columns. The direct-sun DOAS technique used to retrieve NO$_2$ from ground-based Pandora spectrometer measurements has been shown to be highly precise and accurate due to little uncertainty in the path light travels through the atmosphere (i.e., the air mass factor) at solar zenith angles less than 80° (Herman et al., 2009). Thus, Pandora instruments that operate in direct-sun mode are a strong candidate for providing a validation standard for trace gas retrievals from geostationary sensors like TEMPO as well as low-Earth-orbiting sensors like TROPOMI. NASA and the EPA have been working toward creating long-term measurement sites across the

United States to prepare for and aid validation of the satellite products and their usage in air quality management activities (EPA, 2019a). Developments of similar validation site activities are also underway in East Asia and Europe. However, in heterogeneously polluted areas such as cities, the relatively local measurements at such sites may not necessarily be representative of the spatial scales observed by space-based platforms. High-resolution airborne mapping observations provide a unique perspective to assess the impact of spatial-scale mismatches between satellite observations and local validation site measurements.

This work compares high-spatial-resolution NO_2 vertical columns retrieved from GeoTASO to those measured from small networks of Pandora spectrometers operating in direct-sun mode installed in two regions: the western shore of Lake Michigan and the Los Angeles (LA) Basin. The high-spatial-resolution GeoTASO data are then upscaled to spatial resolutions typical of past, present, and planned space-based sensors to demonstrate sensitivity of these comparisons to satellite pixel size in an idealized framework. Finally, these results are compared to two publicly available OMI NO_2 retrievals to provide real-world context. Overall, this work shows the sensitivity of satellite product validation strategies to spatial resolution and begins to demonstrate how the high-spatial-resolution NO_2 data retrieved from airborne mapping observations can be used with planned high-temporal-resolution ground-based column observations to evaluate the influence of spatiotemporal heterogeneity on satellite-based trace gas product validation.

2 Data

2.1 Campaign overview

In 2017, one of NASA's airborne UV–VIS mapping instruments, GeoTASO, was flown aboard the NASA Langley Research Center UC-12b aircraft as part of the Lake Michigan Ozone Study (LMOS; https://www-air. larc.nasa.gov/missions/lmos/index.html, last access: 31 October 2019) and during the Student Airborne Research Program (SARP; https://airbornescience.nasa.gov/content/ Student_Airborne_Research_Program, last access: 31 October 2019). Table 1 summarizes all GeoTASO flights that occurred from 22 May to 27 June 2017. GeoTASO during LMOS was used to characterize the influence of NO_2 emissions and transport on ozone exceedances along the western shore of Lake Michigan. During LMOS, GeoTASO flew on 21 research flights totaling over 90 h. The left map in Fig. 1 shows the areas mapped by GeoTASO during the month-long LMOS campaign in gray. The entire LMOS domain cannot be mapped during a single flight; therefore, individual flight plans focused on subportions of the domain where air quality and meteorological forecasts suggested that science goals could be met for each flight. Eight of the research flights fo-

cused on the city of Chicago, whereas the rest were north of the city along the western shore of Lake Michigan. Each flight lasted approximately 4 h and up to two flights were flown per day (one in the morning and one in the afternoon). Flights were optimized for times where clear skies were expected, and any cloudy scenes that resulted are filtered out for this analysis. The median solar zenith angle for all flights was 36° with a minimum/maximum of 19°/70°.

After LMOS, five research flights were conducted on 26 and 27 June 2017, totaling 15 h, in the Los Angeles Basin during SARP. In 2017, the LA Basin had the highest 8 and 1 h ozone concentrations in the United States, as well as the highest annual mean of NO_2 in the United States (EPA, 2019b). In the LA Basin, a single flight plan was developed to maximize coincidences with Pandora spectrometers installed in the region and extended south to the industrial area near Long Beach, CA (Fig. 1 right). This plan was completed once per flight with up to three flights per day (each flight lasting approximately 3 h). Both flight days in the LA Basin were cloud-free. LA Basin flights spanned a larger range of solar zenith angles than LMOS with a median of 49° and a minimum/maximum of 10°/70°.

One Cimel sun photometer was operating in both study domains during flight days (https://aeronet.gsfc.nasa.gov/ cgi-bin/bamgomas_interactive, last access: 4 November 2018). At the Zion site during LMOS, aerosol optical depth (AOD) was generally below 0.1 on flight days with a peak reported of ∼ 0.2 after cloud filtering. In the LA Basin, there were no data reported for the 26 June 2017 flight day, but AODs were less than 0.1 on 27 June 2017, and both days were similar meteorologically.
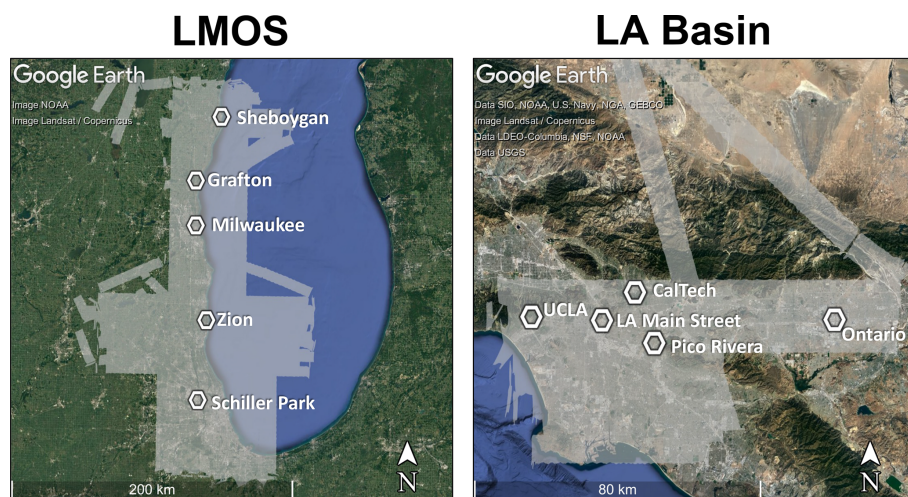
The LMOS region and the LA Basin each had five Pandora instruments operating in direct-sun mode within the research areas during GeoTASO flight days (hexagons in Fig. 1). The number of valid coincidences for each flight are labeled in Table 1. All flight plans had planned overflights of multiple Pandora sites, but cloud cover or instrument issues may have resulted in fewer (or zero) valid coincidences. Pandora site names as well as coordinates and observed pollution ranges during coincidences are listed in Table 2. The locations of these instruments span a wide variety of pollution environments. Urban locations include all those located in the LA Basin and one near the Chicago O'Hare airport (Schiller Park). Pandora spectrometers located along the western shore of Lake Michigan north of Chicago during LMOS were the cleanest (Zion, Milwaukee, Grafton, Sheboygan).

2.2 Pandora

Pandora is a UV–VIS ground-based spectrometer used to retrieve trace gas column amounts (Herman et al., 2009, 2015). Although the instrument has the capability to make both direct-sun and all-sky radiance measurements from which trace gas amounts can be retrieved, only direct-sun retrievals were collected during these campaigns. Direct-sun

Table 1. GeoTASO flight summary.

Flight	Date	Time	Location	SZA range (°)	Pollution scale (95th percentile × 10^{15} molecules cm^{-2})	Percent cloudy pixels	No. of valid Pandora coincidences
1	2017-05-22	12:25–16:20 UTC	Chicago, IL	29–70	12.6	1 %	3
2	2017-05-22	17:40–21:10 UTC	Chicago, IL	21–47	3.6	29 %	1
3	2017-05-27	16:10–19:55 UTC	Zion to Sheboygan	20–33	2.4	3 %	7
4	2017-06-01	13:20–17:05 UTC	Chicago, IL	22–59	17.1	0 %	2
5	2017-06-01	19:05–22:50 UTC	Zion to Sheboygan	26–64	6.8	0 %	7
6	2017-06-02	19:05–23:00 UTC	Zion to Sheboygan	26–66	9.5	0 %	4
7	2017-06-04	19:20–22:35 UTC	Chicago, IL	26–64	10.1	7 %	3
8	2017-06-07	12:55–16:55 UTC	Zion area	23–63	3.4	0 %	4
9	2017-06-07	18:40–22:40 UTC	Zion area	23–62	6.0	0 %	3
10	2017-06-08	12:50–16:35 UTC	Zion area	26–64	5.0	0 %	3
11	2017-06-12	18:55–22:30 UTC	Zion area	24–59	6.0	7 %	1
12	2017-06-13	16:25–19:40 UTC	Chicago, IL	18–29	5.5	9 %	1
13	2017-06-14	13:20–17:00 UTC	Chicago, IL	21–59	5.9	8 %	3
14	2017-06-15	18:50–22:40 UTC	Sheboygan area	22–47	2.1	3 %	2
15	2017-06-15	18:40–22:40 UTC	Sheboygan area	22–61	5.2	2 %	9
16	2017-06-17	16:20–20:20 UTC	Sheboygan area	20–36	0.1	24 %	1
17	2017-06-18	13:20–17:20 UTC	Chicago, IL	21–60	3.2	14 %	2
18	2017-06-19	13:25–17:05 UTC	Chicago, IL	22–58	8.3	25 %	1
19	2017-06-21	13:10–17:05 UTC	Zion to Sheboygan	22–60	7.1	2 %	1
20	2017-06-21	19:00–22:00 UTC	Zion to Sheboygan	24–53	5.7	16 %	0
21	2017-06-26	15:05–17:25 UTC	LA Basin	35–62	25.7	0 %	5
22	2017-06-26	22:40–01:30 UTC	LA Basin	38–70	17.3	0 %	4
23	2017-06-27	14:40–17:10 UTC	LA Basin	37–67	29.8	0 %	5
24	2017-06-27	18:40–21:05 UTC	LA Basin	10–20	17.0	0 %	3
25	2017-06-27	22:40–01:10 UTC	LA Basin	38–70	22.0	0 %	5

Figure 1. Maps of the LMOS and LA Basin regions showing the areas mapped by GeoTASO during summer 2017. The labeled hexagons indicate locations of Pandora spectrometers operating during the flight days. Base map created in © Google Earth Pro.

NO$_2$ columns are reported to have high precision and accuracy, and they are available in near-real time as a standard product. The direct solar beam is measured by Pandora via an optical head sensor attached to a solar tracker. The solar beam is carried to the UV–VIS spectrometer by a fiber optic cable attached to the head sensor. NO$_2$ is retrieved by applying a spectral fitting algorithm (Cede, 2017) using a near-noon reference spectrum, from which the NO$_2$ slant column amount is derived by a statistical calibration approach (Herman et al., 2009). A geometric AMF is used

Pandora site	Latitude, longitude (°)	TropVC range during GeoTASO coincidences $\times 10^{15}$ molecules cm^{-2}
LA Main Street	34.066, −118.227	7.4–28.5
Ontario	34.068, −117.526	7.5–30.1
UCLA	34.074, −118.441	5.0–24.0
Pico Rivera	34.010, −118.069	12.1–18.3
CalTech	34.136, −118.127	3.4–14.2
Sheboygan	43.746, −87.709	−0.9 to 4.3
Grafton	43.343, −87.920	−0.2 to 4.0
Zion	42.468, −87.810	1.5–8.0
Schiller Park	41.965, −87.876	3.5–45.1
Milwaukee	43.061, −87.914	4.1–5.9

for the slant-to-vertical column conversion as the path length through the atmosphere is dominated by the direct solar beam rather than scattered light through the atmosphere (Cede, 2017). The precision and accuracy of the direct-sun NO$_2$ vertical columns are reported as $(2.67 \times 10^{14} / \text{AMF})$ and $(2.67 \times 10^{15} / \text{AMF})$ molecules cm^{-2}, respectively, by Herman et al. (2009). In this work the Pandora retrievals are screened to exclude observations with vertical column error greater than 0.05 DU and normalized rms greater than 0.005, to limit the retrieval uncertainty to approximately 10 %.

2.3 Ozone Monitoring Instrument (OMI)

OMI is a space-based UV–VIS instrument launched in 2004 aboard the EOS-Aura satellite in a sun-synchronous orbit with an Equator crossing time in the early afternoon (Levelt et al., 2006). This work uses the NASA standard product (SP) version 3 (Krotkov et al., 2017) and the Berkeley High Resolution (BEHR) product (Russell et al., 2011; Laughner et al., 2018b, 2019) to assess how their tropospheric column retrievals compare with measurements from Pandora spectrometers deployed during summer 2017 in the LMOS and the LA Basin domains.

The two vertical column products are based on the same slant columns (produced by the SP retrieval), but they differ in their a priori inputs for the tropospheric air mass factor calculation. As the name suggests, BEHR a priori assumptions have a higher spatial resolution than the NASA SP (Russell et al., 2011; Bucsela et al., 2013; Krotkov et al., 2017; Laughner et al., 2018a, 2019). Both products use monthly NO$_2$ a priori profile assumptions, but NASA SP V3 profiles are at a spatial resolution of 1° latitude by 1.25° longitude from the Global Modeling Initiative chemical transport model, whereas BEHR profiles are from a WRF-Chem model sim-

ulation at 12 km resolution. Assumptions about surface reflectivity in the NASA SP are from an OMI-based climatology at 0.5° × 0.5° (Kleipool et al., 2008), and the BEHR product uses a bidirectional reflectance factor from the Moderate Resolution Imaging Spectroradiometer (MODIS) over land at 30 arcsec resolution and an ocean reflectivity model over water. Terrain pressure in BEHR is assumed from WRF-Chem pressure profiles adjusted with the Global Land One-kilometer Base Elevation database (Hastings and Dunbar, 1999) and the hypsometric equation, whereas the NASA SP uses a 3 km digital elevation model (Boersma et al., 2011).

OMI data used in this analysis are filtered to exclude cloud fractions (derived from MODIS) greater than 20 % (following criteria defined in Laughner et al., 2019) and data from OMI's row anomaly (http://projects.knmi.nl/omi/research/product/rowanomaly-background.php, last access: 31 October 2019). From 2004 until October 2017, OMI had the finest spatial resolution of any NO$_2$-retrieving sensor in low Earth orbit. Before the appearance of the row anomaly in 2007, the finest pixel size of OMI was approximately 13 km × 24 km at nadir. In January 2009, the row anomaly extended to affect nadir pixels, and during summer 2017 the pixel areas coincident with the Pandora campaign observations ranged from 365 km^2 near-nadir to approximately 4600 km^2 at the edge of the swath.

2.4 GeoTASO

Geostationary Trace gas and Aerosol Sensor Optimization (GeoTASO) is a hyperspectral mapping instrument built by Ball Aerospace (Leitch et al., 2014) to acquire data for optimizing and testing new high-resolution retrievals of trace gases (NO$_2$, O$_3$, and HCHO) and aerosols in preparation for geostationary air quality observations. The instrument is composed of a reflective telecentric telescope that focuses scattered light within its field of view through a photoelastic modulator for depolarization and lastly into an Offner spectrometer. Within the spectrometer the second-order and first-order diffracted beams are used to form the ultraviolet (UV) and visible (VIS) spectral ranges, respectively. Each spectral range (UV: 300 to 380 nm, and VIS: 410 to 690 nm) is focused onto separate two-dimensional charge coupled devices (CCDs) (1056 pixels in the wavelength dimension by 1033 pixels in the spatial dimension) operated at an integration time of 250 ms for all flights. NO$_2$ is retrieved using a spectral window within the VIS channel, which has a spectral resolution (FWHM) of 0.88 nm and a spectral sampling of 3.1 pixels (Nowlan et al., 2016). GeoTASO observes as a push-broom sensor with an across-track nadir field of view of 45°, providing a swath width of approximately 7 km from a nominal altitude of 8.5 km. Spectra ($\sim$ 300 images) are coadded to an approximate ground pixel size of 250 m × 250 m.

During GeoTASO flights, gapless maps (otherwise referred to as rasters) were created over an area of interest by executing flight plans composed of parallel flight legs spaced

6 km apart. The overlap in swath between these flight legs provided a tolerance for maintaining gapless coverage during instances of strong crosswinds or when a lower flight altitude was selected in order to operate below high-level thin cirrus clouds. This raster strategy provides data that can easily be spatially coadded to evaluate the influence of spatial resolution on tropospheric NO$_2$ column measurements, as is shown herein. Additional details and estimated uncertainties of the GeoTASO NO$_2$ retrieval are elaborated in the following sections.

2.4.1 Airborne NO$_2$ slant column retrieval and uncertainty

NO$_2$ differential slant columns (DSCs) are retrieved using QDOAS, an open-source DOAS computing software developed by the Royal Belgian Institute for Space Aeronomy (http://uv-vis.aeronomie.be/software/QDOAS, last access: 31 October 2019). Fitted trace gas and interference cross sections include NO$_2$ (Vandaele et al., 1998), O$_4$ (Thalman and Volkamer, 2013), H$_2$O (Rothman et al., 2009), CHOCHO (Volkamer et al., 2005), Ring spectrum (Chance and Kurucz, 2010), and a fifth-order polynomial in the spectral window of 425–460 nm. The resultant DSCs can be physically described as the additional total NO$_2$ absorption along the path sunlight travels through the atmosphere to the GeoTASO instrument relative to the reference atmosphere.

Reference spectra are collected in-flight using nadir-viewing observations for each across-track position in the swath over a homogeneous area with minimal NO$_2$ absorption. One reference set was collected for each region. The LMOS reference spectrum was observed during nadir observations on 27 May 2017 at 19:00 UTC (SZA = 35°) over Lake Michigan with an estimated below-aircraft column of 2.3×10^{15} molecules cm^{-2} (estimated from the NAM-CMAQ model described below). For the LA Basin flights, the reference was collected over a clean homogeneous area north of the LA Basin on 27 June 2017 also at 19:00 UTC (SZA = 16°) with an estimated below-aircraft column of approximately 1×10^{15} molecules cm^{-2}.

The average spectral fitting uncertainty for the NO$_2$ DSCs over all flights is 1.2×10^{15} molecules cm^{-2} with a standard deviation of 0.25×10^{15} molecules cm^{-2}. Higher solar zenith angles (SZA) and lower surface albedos both result in slightly higher uncertainties due to their impacts on instrument signal-to-noise ratio. A multilinear regression applied to the dependent variable of NO$_2$ DSC uncertainty vs. the independent variables of SZA and surface albedo, for all cloud-free data, indicates that 33 % of the variability in DSC uncertainty is associated with changes in SZA (uncertainty increases with increasing SZA by 0.011×10^{15} molecules cm^{-2} per degree) and almost 15 % is associated with variations in surface albedo (uncertainty increases with decreasing albedo by 0.033×10^{15} molecules cm^{-2} per 0.01 decrease in albedo). Additional uncertainty due to using one NO$_2$ absorption

cross section at a single temperature (294 K) leads to a potential bias of -0.6 ± 1.7 %, estimated using the NO$_2$ profile weighted effective temperature profile in Eq. (4) in Bucsela et al. (2013).

2.4.2 Slant-to-vertical column conversion

Further processing of DSCs into vertical columns (VCs) requires computations of the AMF: the ratio of the pathlength of light through the atmosphere due to scattering and geometry to the vertical pathlength. AMFs depend on a priori assumptions such as the vertical distribution of NO$_2$, surface reflectivity, clouds, aerosols, sun angle, and viewing geometry (Palmer et al., 2001; Lamsal et al., 2017). Mathematically, AMFs are the integrated product of (1) scattering weights (the vertical distribution of the instrument sensitivity calculated by a radiative transfer model) and (2) the NO$_2$ profile shape factor (the relative vertical distribution of NO$_2$) (Palmer et al., 2001). Scattering weight calculations are most sensitive to inputs that influence light transmission through the atmosphere, most notably from solar and viewing geometry, surface reflectivity, and aerosols (Lamsal et al., 2017; Meier et al., 2017). This work uses the Harvard Smithsonian Astrophysical Observatory's AMF tool, which packages the VLIDORT radiative transfer model to calculate scattering weights (Spurr, 2006; Nowlan et al., 2016, 2018). Inputs include atmospheric profiles of temperature, pressure, ozone, NO$_2$, aerosol, aircraft altitude, viewing geometry, solar geometry, and surface reflectance.

Tropospheric NO$_2$ profiles are taken from a 12 km hourly analysis of a parallel developmental simulation of the North American Model–Community Multiscale Air Quality (NAM-CMAQ) model from the National Air Quality Forecasting Capability (NAQFC; Stajner et al., 2011). Stratospheric profiles are estimated using the PRATMO chemical box model of stratospheric NO$_2$ profile climatology (Prather, 1992; McLinden et al., 2000), which estimates NO$_2$ between approximately 10 and 60 km as a function of month, latitude, and solar zenith angle. This stratospheric model has been used in previous GeoTASO retrievals and has an estimated uncertainty of ~ 30 % in the stratospheric column (Bourassa et al., 2011; Nowlan et al., 2016). Temperature and pressure profiles from the NAM-CMAQ in the troposphere and the Realtime Air Quality Modeling System (RAQMS; Pierce et al., 2009) up to 60 km are extracted and merged, and ozone profiles are extracted from the NAM-CMAQ analysis for the troposphere and OMI gridded monthly climatology in the stratosphere (Liu et al., 2010) for May and June 2017.

Noguchi et al. (2014) evaluated the influence of surface anisotropy on NO$_2$ AMFs for geostationary-scale measurements using a 1 km MODIS BRDF product and found that not accounting for BRDF in the AMF calculation, especially in areas with high NO$_2$ near the surface, can lead to large errors. For this reason, this work uses the BRDF isometric, volumetric, and geometric kernels retrieved in band 3 by the

MODIS MCD43A1 daily L3 500 m v006 product (Lucht et al., 2000; Schaaf and Wang, 2015). To fill gaps and decrease noise, the daily product is averaged over a month in the regions GeoTASO measured (22 May–21 June for LMOS and 15 June–14 July for the LA Basin). The remaining gaps are small and are filled using linear interpolation of nearby pixels. Variations in BRDF-derived albedo compare well with the brightness of surface features. Li et al. (2018) found that the v006 MCD43A1 product compared very well with Multi-angle Imaging SpectroRadiometer (MISR) land surface reflectance with little bias and a high correlation ($r = 0.95$ in a case study in northeast Asia).

Clouds and aerosols are not considered in the AMF calculation in this work, as cloudy scenes are filtered by removing pixels having detector count rates of greater than 2.5×10^4 counts s^{-1} within the DOAS NO₂ spectral window, and aerosol loading was relatively low during flight days. Given the relatively low aerosol loadings, errors in AMF due to neglecting aerosols are expected to be small for these flights ($< 5\%$ using sensitivities shown by Lamsal et al., 2017).

Differential slant columns are converted into below-aircraft vertical columns using the following equation:

$$\text{VC}_{\text{below}}\text{or}\text{TropVCs}$$
$$= \frac{\text{DSC} - \text{VC}_{\text{above}}\text{AMF}_{\text{above}} + \text{reference slant column}}{\text{AMF}_{\text{below}}}, \quad (1)$$

where DSC is the differential slant column, VC$_{\text{above}}$ and VC$_{\text{below}}$ are respectively the vertical column above and below the aircraft, and AMF$_{\text{above}}$ and AMF$_{\text{below}}$ are respectively the calculated AMF above and below the aircraft. As NO₂ column variations in the troposphere are largely confined to the boundary layer, this work assumes that residual tropospheric variations in the above-aircraft column are negligible, and the below-aircraft vertical columns are referred to as tropospheric vertical columns (TropVCs).

2.4.3 Vertical column retrieval sensitivity and uncertainty

Figure 2 shows examples of NO₂ TropVCs (panels a and b) and tropospheric AMFs (panels c and d) for a morning flight ($\sim$ 08:30–12:00 LDT) over Chicago, IL, on 1 June 2017 (left) and a morning flight ($\sim$ 08:40–10:05 LDT) over the LA Basin from 26 June 2017 (right). Figure 2e and f shows base maps from Google Earth Pro to aid identification of surface features in the maps above. In the areas mapped in Fig. 2, NO₂ TropVC spans roughly 2 orders of magnitude, and spatial patterns are consistent with emission sources, such as busy roadways, airports, and industrial regions. Both mornings in each region had relatively stagnant conditions.

Over land, large spatial variations of tropospheric AMF are evident and associated primarily with the surface reflectance characteristics. A multivariable linear regression of these data indicates that surface albedo explains 64 % of the variability in tropospheric AMF, illustrating the importance of accurately treating surface reflectance in these high-spatial-resolution retrievals. Over an area with homogeneous surface reflectance (like Lake Michigan east of Chicago), the subtle influence of a varying NO₂ shape factor is visible in the AMF but has little impact on the magnitude of TropVC because there is little NO₂ in this location. The a priori NO₂ profile accounts for 16 % of the variability in tropospheric AMF. Viewing geometry has smaller effects, with SZA accounting for 1.8 % of the variability and the relative azimuth angle and viewing zenith angle causing even smaller amounts.

To better gauge the sensitivity of AMF and TropVC to the NO₂ vertical profile in the troposphere, the AMFs calculated for the most polluted LMOS flight (1 June 2017; Fig. 2) were compared to AMFs calculated using a single median NAM-CMAQ NO₂ vertical profile (not shown). This median profile is representative of a moderately polluted urban area with a tropospheric NO₂ column of 3.6×10^{15} molecules cm^{-2}, most of the NO₂ in the lowest kilometer of the atmosphere, and an NO₂ maximum at the surface of approximately 4 ppbv. The resulting differences in AMF can be large, ranging from -30% to 10 %; however, the largest AMF differences occur over relatively clean areas in which the median polluted profile shape is less representative. The differences in TropVCs are about $\pm 1 \times 10^{15}$ molecules cm^{-2} at the 5th/95th percentiles, with 50 % of the points having differences between -0.2×10^{15} and 0.5×10^{15} molecules cm^{-2}. These values are on the same order of magnitude as the uncertainty in DSCs.

To estimate total uncertainty in the TropVC, error propagation was applied to Eq. (1). Assuming a 50 % uncertainty in the NAM-CMAQ profile, 30 % in the PRATMO profiles, and a conservative 30 % uncertainty in the below-aircraft AMF (the largest percent variation in the sensitivity study discussed in the preceding paragraph), the uncertainty in the reference slant column is estimated to be 2.3×10^{15} molecules cm^{-2} for LMOS and 1.9×10^{15} molecules cm^{-2} for SARP. The average uncertainty in the above-aircraft vertical column is 1.3×10^{15} molecules cm^{-2} with a standard deviation of 0.08×10^{15} molecules cm^{-2}. The median total uncertainty for TropVCs for both regions combined is 2.3×10^{15} molecules cm^{-2}. Percent uncertainty (5th–95th percentile) ranges from 46 to 143 % for relatively unpolluted columns ($< 5 \times 10^{15}$ molecules cm^{-2}), from 32 to 60 % for moderately polluted columns (5–15×10^{15} molecules cm^{-2}), and $\sim$ 30 % for polluted columns ($> 15 \times 10^{15}$ molecules cm^{-2}). These values are similar to those calculated by Nowlan et al. (2016).
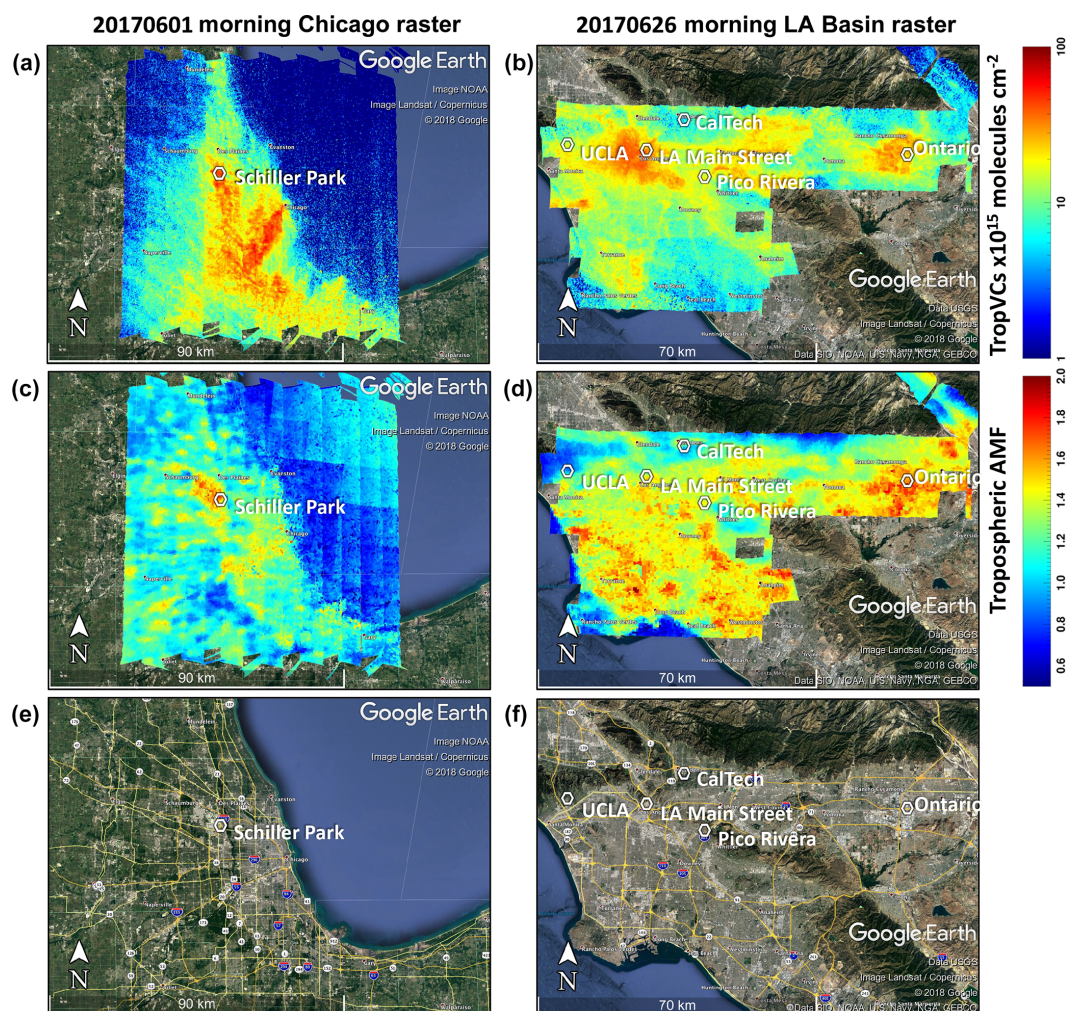
Figure 2. Tropospheric NO$_2$ vertical column on a log$_{10}$ color scale **(a, b)**, tropospheric AMF on a linear color scale **(c, d)**, and base map **(e, f)** for a Chicago raster on the morning (08:30–12:00 LDT) of 1 June 2017 **(a, c, e)** and an LA Basin raster on the morning (08:40–10:05 LDT) of 26 June 2017 **(b, d, f)**. The base maps show roadways, urbanized areas, and surface characteristics. The labeled hexagons indicate locations of Pandora spectrometers. Base map created in © Google Earth Pro.

3 Results

3.1 Comparison of airborne GeoTASO and ground-based Pandora retrievals

Pandora spectrometer measurements have been previously used to validate retrieval products from GeoTASO and similar airborne mapping spectrometers during intensive campaigns (Nowlan et al., 2016, 2018; Lamsal et al., 2017). Figure 3 shows the comparison between the 80 coincident Pandora and GeoTASO TropVC observations during LMOS and the LA Basin flights colored by ground site. The first five ground sites in the legend correspond to Pandora spectrometers installed in the LA Basin, and the last five are located in the LMOS domain. Coincidences are identified as the median of all cloud-free GeoTASO TropVCs having pixel centers within a 750 m radius of a Pandora spectrometer site

for each overpass (minimum requirement of 16 valid cloud-free GeoTASO 250 m × 250 m pixels for a spatial coverage of at least 1 km^2) and the Pandora column observed closest in time to the GeoTASO overpass (within ±5 min). A Pandora TropVC is derived by subtracting the stratospheric vertical column calculated with the PRATMO climatology from the Pandora total column, following the same approach used with GeoTASO TropVCs. Coincidences without at least two valid Pandora data points within ±5 min of the GeoTASO overpass are excluded because acquisition of only a single Pandora data point within 10 min indicates likely periodic clouds or poor solar tracking by the instrument. TropVCs from GeoTASO compare well with Pandora, with a high correlation ($r^2 = 0.91$), a slope of 1.03, and an offset of 0.52×10^{15} molecules cm^{-2}.
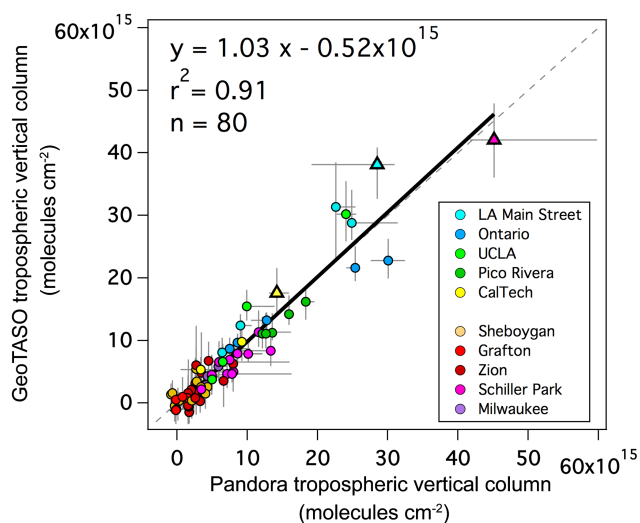
Figure 3. Scatter plot of GeoTASO NO$_2$ TropVCs vs. Pandora NO$_2$ TropVCs colored by Pandora site. Vertical whiskers show the 90th and 10th percentiles of GeoTASO TropVCs within the 750 m radius of the Pandora site. Horizontal whiskers show the maximum and minimum Pandora TropVCs within the ± 5 min coincidence window. Triangles indicate coincidences discussed within Sect. 3.1. The gray dashed line indicates the 1 : 1 line.

The whiskers in Fig. 3 indicate the 10th and 90th percentiles of GeoTASO TropVCs within the 750 m radius for GeoTASO (vertical whiskers) and the maximum and minimum Pandora TropVC within ± 5 min from the GeoTASO overpass (horizontal whiskers, representing six to seven valid Pandora measurements for most of these coincidences), providing a glimpse of the spatiotemporal variability at the time of the coincidence. Generally, spatial variability (vertical whiskers) increases as the magnitude of NO$_2$ increases. An exception to this pattern occurs at the Zion site. Zion has the lowest surface albedo of any site, ranging from 1.3 % to 2.6 % depending on SZA. The lower albedo over the Zion region together with the relatively low NO$_2$ amounts leads to a lower signal-to-noise ratio in the GeoTASO observations, resulting in a higher uncertainty in the DOAS spectral fit (as discussed in Sect. 2.1). Therefore, the large vertical whiskers at this site are indicative of increased uncertainty in the retrieval in addition to spatial heterogeneity.

The largest temporal variability (horizontal whiskers) occurs at the Schiller Park site in Chicago, IL, which is located along a major highway near the end of a Chicago O'Hare airport runway. High temporal variability is common at the site and is likely due to local emissions associated with air traffic and nearby roadways. The most polluted point of all coincidences occurs at Schiller Park on 1 June 2017 (pink triangle in Fig. 3), and this case is further explored in Fig. 4. Figure 4a shows a map of the GeoTASO NO$_2$ TropVCs and a hexagon depicting the Pandora location, which is colored by the NO$_2$ column observed by Pandora nearest in time to the GeoTASO

overpass. The 750 m radius used to define coincident Geo-TASO data and an arrow depicting the direction in which Pandora is observing are overlaid. GeoTASO observed a median of 42×10^{15} molecules cm^{-2}, whereas Pandora observed 45×10^{15} molecules cm^{-2}. Inside the 750 m radius, NO$_2$ columns range between 30 and 50×10^{15} molecules cm^{-2}, and the highest columns observed occur along the viewing direction of Pandora. Figure 4b shows a time series of the Pandora TropVC surrounding this overpass and the Geo-TASO coincidence. Within an hour prior to the overpass, large temporal variations in NO$_2$ column are observed by Pandora, suggestive of small-scale plumes influencing the site. In the 10 min Pandora window (gray section), Pandora peaks at over 60×10^{15} molecules cm^{-2}. If any temporal averaging is applied to Pandora data in this case, the coincidence would yield a larger apparent difference between Geo-TASO and Pandora. The tremendous amount of variability at this highly heterogeneous location suggests caution for use in applications such as satellite validation.

Although the 80 GeoTASO/Pandora coincidences are highly correlated with a slope near 1 : 1, there are a few outliers that deviate from the linear regression line by amounts larger than the range of observed variability by either instrument. Some of these outliers can be attributed to mismatches in spatial representativeness, as the viewing geometry of the Pandora spectrometer is always oriented in the direction of the sun while the GeoTASO median is constructed from pixels within the 750 m radius centered on the Pandora location extending into all directions. Figure 5 highlights one of these cases (yellow triangle in Fig. 3). Over the CalTech site in the LA Basin on 27 June 2017, Pandora observes a column of approximately 14×10^{15} molecules cm^{-2}, whereas the GeoTASO spatial median is 18×10^{15} molecules cm^{-2}. The GeoTASO TropVC map (Fig. 5a) shows that Pandora is observing in a direction where NO$_2$ values are at a local minimum, such that the GeoTASO median within the 750 m radius is about 30 % higher than Pandora, though Geo-TASO TropVCs along the viewing direction of Pandora at that time are more similar to the Pandora observations. Pandora TropVCs are varying slowly in time surrounding the GeoTASO overpass (Fig. 5b). Together these characteristics suggest that the differences between these two observations are more likely associated with the spatial criteria assumed for this comparison rather than the temporal variability near the coincidence time. Some of the other coincidences showing notable differences, including the two most polluted Ontario points (both lying below the 1 : 1 line with concentrations of $20–25 \times 10^{15}$ molecules cm^{-2}), also appear to be associated with the assumption in spatial criteria (not shown). Future comparisons of Pandora direct-sun retrievals to high-spatial-resolution airborne data could consider Pandora's viewing geometry in the coincidence criteria, but this is not a viable option for validating satellite products that are not as spatially refined
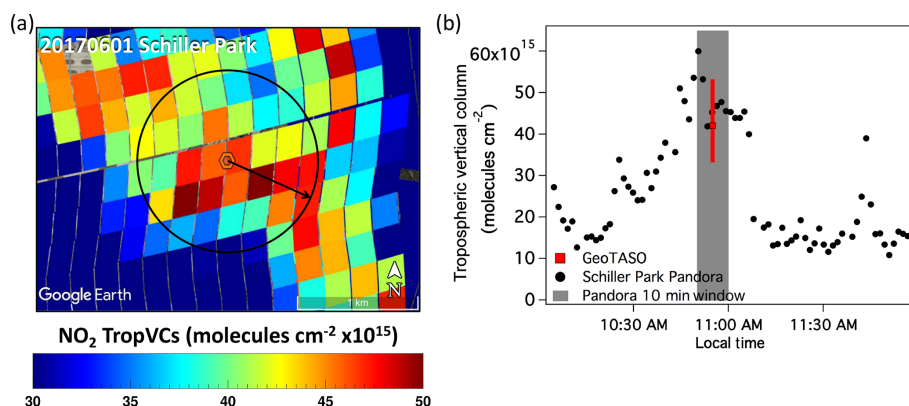
Figure 4. (a) Map of GeoTASO TropVCs on a linear color scale for the Schiller Park overflight on 1 June 2017 at 15:55 UTC (10:55 LDT) (pink triangle in Fig. 3) with the 750 m radius considered in the spatial binning of GeoTASO overlaid and an arrow depicting the Pandora viewing direction (solar azimuth angle) during the overpass time. The Pandora hexagon is colored by the NO₂ TropVC measured by Pandora during the overpass. **(b)** Time series showing Pandora data (black points) within approximately ±1 h of the GeoTASO overpass. The Pandora temporal window for the coincidence is shaded in gray, and the GeoTASO TropVC and 10th–90th percentiles from the overpass are shown in red. Base map created in © Google Earth Pro.

Figure 5. (a) Map of GeoTASO TropVCs on a linear color scale for the CalTech overflight on 27 June 2017 at 16:41 UTC (09:41 LDT) (yellow triangle in Fig. 3) with the 750 m radius considered in the spatial binning of GeoTASO overlaid and an arrow depicting the Pandora viewing direction (solar azimuth angle) during the overpass time. The Pandora hexagon is colored by the NO₂ TropVC measured by Pandora during the overpass. **(b)** Time series showing Pandora data (black points) within approximately ±1 h of the GeoTASO overpass. The Pandora temporal window for the coincidence is shaded in gray, and the GeoTASO TropVC and 10th–90th percentiles from the overpass are shown in red. Base map created in © Google Earth Pro.

The largest outlier from the regression line of Pandora-to-GeoTASO coincidences occurs at LA Main Street on the afternoon of 27 June 2017 (blue triangle in Fig. 3), where Geo-TASO observes a TropVC of 38×10^{15} molecules cm^{-2} and the Pandora TropVC is only 28×10^{15} molecules cm^{-2}. This coincidence also shows large gradients both spatially and temporally. What is unique about this case is the environmental/meteorological conditions present during this time period that make data comparisons and GeoTASO retrieval challenging. Figure 6 has the same formatting as Figs. 4 and 5. Focusing on the 10 min window used in the temporal matching of Pandora data, Pandora NO₂ TropVC increases from 20×10^{15} molecules cm^{-2} to over 30×10^{15} molecules cm^{-2}. This feature is caused by the arrival of a sea breeze front

passing through from the southwest at this time that acts as a convergence zone accumulating NO₂ along this front as it passes through the LA Basin (Judd et al., 2018). In this case, because the Pandora data show a rapid increase, any temporal averaging window placed on the Pandora data for data comparison would not be representative of the conditions during the overpass (similar to the coincidence shown in Fig. 4). Pandora reaches a peak within this 10 min window of 31×10^{15} molecules cm^{-2} approximately 1 min after the GeoTASO overpasses, which is closer to the magnitude observed by GeoTASO but still about 7×10^{15} molecules cm^{-2} lower. Within 5 to 10 min after the overpass, Pandora values rise again to a range of $33–37 \times 10^{15}$, almost as large as the GeoTASO median value.
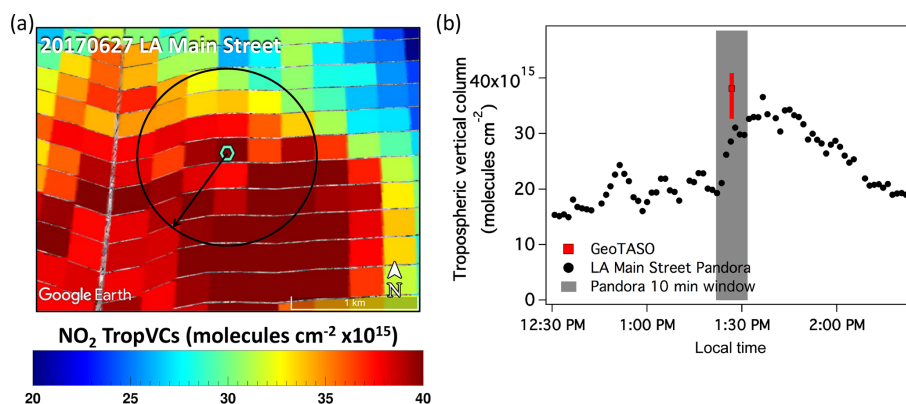
Figure 6. (a) Map of GeoTASO TropVCs on a linear color scale for the LA Main Street overflight on 27 June 2017 at 20:26 UTC (13:26 LDT) (cyan triangle in Fig. 3) with the 750 m radius considered in the spatial binning of GeoTASO overlaid and an arrow depicting the Pandora viewing direction (solar azimuth angle). The Pandora hexagon is colored by the NO₂ TropVC measured by Pandora during the overpass. **(b)** Time series showing Pandora data (black points) within approximately ±1 h of the GeoTASO overpass. The Pandora temporal window for the coincidence is shaded in gray, and the GeoTASO TropVC and 10th–90th percentiles from the overpass are shown in red. Base map created in © Google Earth Pro.

Figure 6a indicates that directionality does not reconcile the observations as GeoTASO NO₂ TropVCs in the direction Pandora is viewing are consistently larger than Pandora observations, suggesting a potential high bias in the GeoTASO TropVC in this case. High bias could be caused by an underestimation of the AMF; the tropospheric AMF would have to increase from 1.3 to ∼ 1.75 for this area to yield a TropVC similar to Pandora. Given the unique circumstances of the sea breeze front, and the relatively coarse resolution of the NAM-CMAQ model used to obtain the NO₂ profile (12 km), we speculate that perhaps the shape factor used in the AMF calculation may not be representative of the actual NO₂ vertical profile within the sea breeze circulation during this time. The rapid fluctuations in Pandora observations through this period also suggest that the air mass is not well mixed; i.e., eddies likely exist in the vicinity of this front, which could affect vertical structure at very localized scales. Another contribution could be inaccuracies in the AMF associated with surface reflectance at this site. All LA Main Street coincidences lie above the 1 : 1 line in Fig. 3 (GeoTASO TropVC is consistently larger than Pandora), which could be caused by a low bias in the BRDF weighting kernels. LA Main Street is in an area that has fewer valid retrievals from the MCD43A1 product during the monthly average used for BRDF input to VLIDORT. Further investigation of systematic biases by site due to BRDF uncertainty would require more consistent sampling at the site, which will be possible with satellite products and long-term Pandora measurements used for product validation in the future.

3.2 Scaling GeoTASO to satellite product footprints

Past, present, and planned satellite instruments have spatial resolutions that are coarser than the GeoTASO airborne measurements. The gapless mapping strategy executed with GeoTASO during summer 2017 provides fine-resolution data suitable for averaging to coarser areal resolutions typical of these current and next-generation satellite retrievals. As demonstrated by the good agreement between Pandora and GeoTASO shown in Sect. 3.1, the GeoTASO observations during these rasters capture the spatiotemporal variability existing in these areas. Comparisons of upscaled GeoTASO retrievals with Pandora measurements provide an early assessment of the capabilities of the next-generation sensors for resolving urban-scale NO₂ and also give insight toward validation strategies in urban regions, where subpixel variability within the satellite product footprint may be significant.

To simulate the satellite products, each GeoTASO raster is averaged to fixed grids with pixel areas representative of near-nadir observations from TEMPO, TROPOMI, and OMI. These grids are simplified by making each pixel square in shape to avoid introducing an orientation bias. Simulated pixels are $3\,km \times 3\,km$ $(9\,km^2)$ for TEMPO (literature reported $9.24\,km^2$ per pixel, Zoogman et al., 2017), $5\,km \times 5\,km$ $(25\,km^2)$ for TROPOMI (literature reported $24.5\,km^2$, van Geffen et al., 2019), and $18\,km \times 18\,km$ $(324\,km^2)$ for OMI (FoV75Area for nadir is $338.4\,km^2$).

GeoTASO data are remapped to these fixed grids by computing a weighted average of the GeoTASO TropVCs based on the areal overlap within each simulated satellite grid pixel for each raster. Figure 7 shows an example of this process for the midday Los Angeles raster on 27 June 2017, at the nominal GeoTASO resolution and each simulated satellite product resolution. At this time, a marine–land air mass convergence zone was created by the development of a sea breeze that resulted in an accumulation of NO₂ seen as a line of enhanced NO₂ in excess of 30×10^{15} molecules cm⁻² extending north and south of LA Main Street (discussion of Fig. 6,
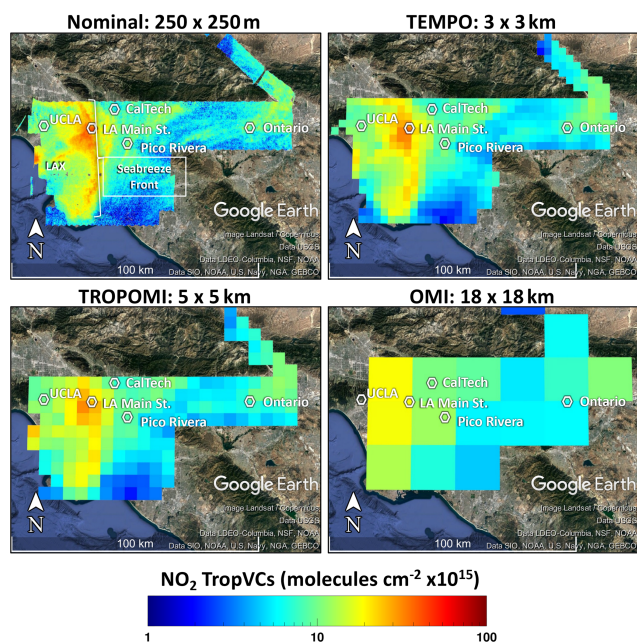
Figure 7. Maps of GeoTASO NO$_2$ TropVC on a log$_{10}$ color scale averaged to the labeled pixel sizes to demonstrate the spatial detail that would be observed from the midday raster in Los Angeles on 27 June 2017. All pixels shown have at least 30 % of their area mapped by GeoTASO during this timeframe. Base map created in © Google Earth Pro.

Figure 8. Maps of GeoTASO NO$_2$ TropVC on a log$_{10}$ color scale averaged to the labeled pixel sizes to demonstrate the spatial detail that would be observed from the midday raster in the Chicago area on 22 May 2017. All pixels shown have at least 30 % of their area mapped by GeoTASO during this timeframe. Base map created in © Google Earth Pro.

Sect. 3.1; Judd et al., 2018). A plume is also seen extending inland from the Los Angeles International Airport (LAX). As expected, fine-scale features evident in the native GeoTASO observations are increasingly blurred as the spatial resolution is degraded. The airport plume is spatially distinct up to the TEMPO spatial scale, and the sea breeze is resolved through the TROPOMI spatial scale, but neither are visible at the spatial scale of OMI.

Another example is shown in Fig. 8 for a Chicago raster near midday on 22 May 2017. In this example, the southwesterly wind throughout the day quickly advected local emissions out over Lake Michigan, allowing visualization of fresh emission source regions and broadening and accumulation of the resulting pollution plume as it passes over the Chicago metropolitan area. The native-resolution GeoTASO retrievals show three areas of enhanced NO$_2$: near Schiller Park–O'Hare airport; central Chicago; and the industrial shore near South Chicago and Gary, IN. This raster was repeated three other times on this day, and all four rasters show a similar spatial pattern, but magnitude of NO$_2$ TropVCs decreases throughout the day, likely indicating that morning emissions are larger than afternoon emissions on this day (not shown). These spatial features are discernible up through the areal resolution of TROPOMI, but the OMI spatial scale is larger than the physical separation of these three enhanced regions, leading to loss of this spatial infor-
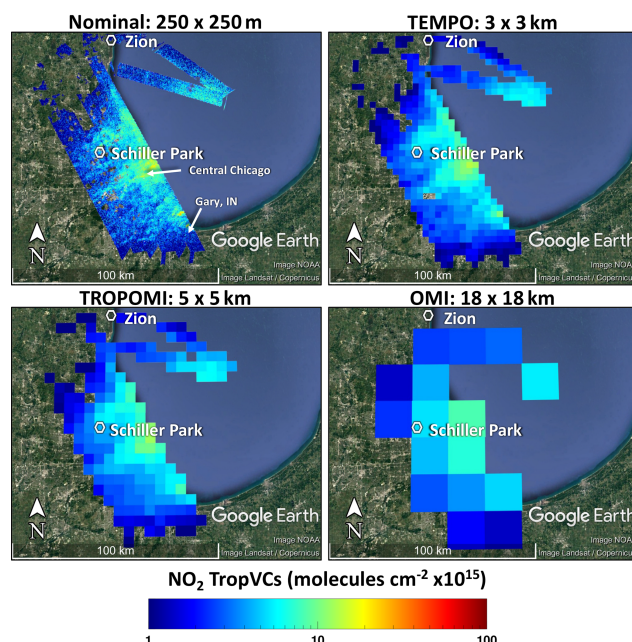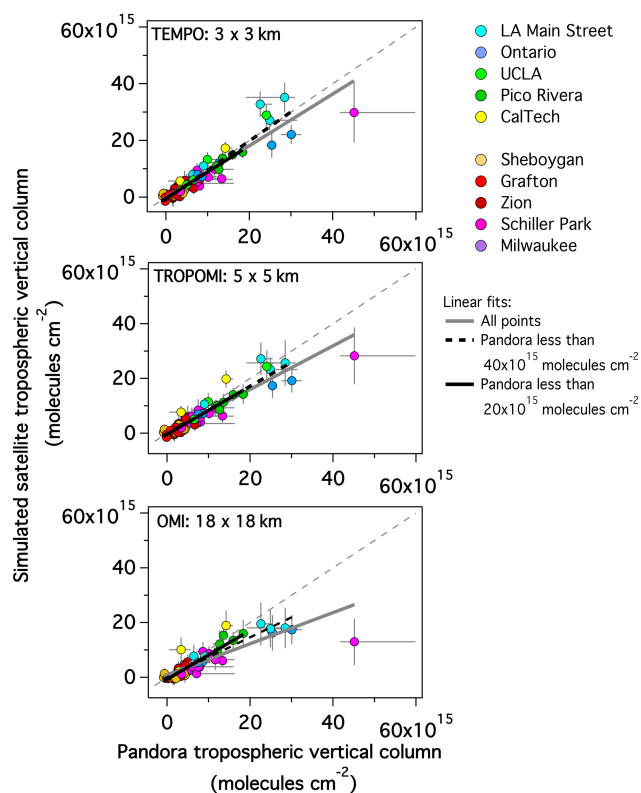
mation. The maximum TropVC observed at an OMI spatial resolution is even displaced, such that it does not accurately represent the location of the highest NO$_2$ TropVCs.

This upscaling technique was applied to all GeoTASO flights listed in Table 1. To assess the impact of spatial resolution on comparisons to Pandora, each Pandora coincidence from Sect. 3.1 is matched to its equivalent upscaled pixel. Figure 9 shows the scatter plots of these coincidences, and the associated linear regression statistics are shown in Table 3. To avoid excess extrapolation, only upscaled grid cells that are at least 30 % sampled by GeoTASO are considered in this analysis, which is why the number of coincidences decrease as pixel size increases (Table 3).

Increasing pixel size progressively worsens 1 : 1 Pandora agreement, with the slope decreasing from 1.03 at native resolution to 0.88, 0.77, and 0.57, respectively, at TEMPO, TROPOMI, and OMI scales. The decrease in slope is partially driven by the most polluted coincidence at Schiller Park. Figure 10 shows this coincidence in context (zoomed out map from Fig. 4) with the upscaled equivalent pixels from TEMPO, TROPOMI, and OMI overlaid. The two nearest TEMPO pixels are shown because the Pandora location is near a pixel edge, just inside the left TEMPO pixel. The GeoTASO observations show that the Pandora spectrometer is located within a narrow region of strongly enhanced NO$_2$. The size of the feature observed by GeoTASO and Pandora

Table 3. Statistics between Pandora and the GeoTASO data at the nominal pixel size shown in Fig. 3 as well as the simulated pixel sizes for TEMPO, TROPOMI, and OMI products shown in Fig. 9.

	All points				Pandora $< 40 \times 10^{15}$ molecules cm^{-2}				Pandora $< 20 \times 10^{15}$ molecules cm^{-2}			
Pixel size	Slope	Intercept $\times 10^{15}$	r^2	N	Slope	Intercept $\times 10^{15}$	r^2	N	Slope	Intercept $\times 10^{15}$	r^2	N
Nominal:	1.03	0.52	0.91	80	1.08	−0.75	0.89	79	0.96	−0.30	0.84	73
TEMPO: 3 km × 3 km	0.88	−0.07	0.86	79	1.03	−0.72	0.89	78	0.93	−0.35	0.85	72
TROPOMI: 5 km × 5 km	0.77	0.11	0.88	76	0.88	−0.32	0.89	75	0.87	−0.36	0.81	69
OMI: 18 km × 18 km	0.57	0.9	0.61	66	0.73	0.01	0.83	65	0.89	−0.7	0.78	60

Figure 9. Scatter plot of GeoTASO TropVCs scaled to the nadir areal resolution of TEMPO **(a)**, TROPOMI **(b)**, and OMI **(c)** TropVCs vs. Pandora TropVCs colored by site and their associated linear fits (statistics listed in Table 3). Vertical bars show standard deviation of GeoTASO TropVCs within the upscaled pixel. Horizontal bars show the minimum and maximum of Pandora data within the ±5 min coincidence window. The gray dashed line indicates the 1 : 1 line.

in this case is smaller than the spatial scale of TEMPO pixels, and because the TEMPO pixels also include regions of much lower NO₂ values, the simulated satellite values decrease from 42×10^{15} molecules cm^{-2} at native GeoTASO resolution to less than 30×10^{15} molecules cm^{-2} at simulated TEMPO resolution. This case illustrates the challenge of determining the difference between retrieval bias and spatial misrepresentation but also the advantage of having

high-spatial-resolution airborne spectrometer observations as a transfer standard between satellite measurements and localized column measurements from Pandora. In this analysis, the native-resolution retrieval does not appear to be biased (Sect. 3.1). Therefore, the changes in the relationship between upscaled GeoTASO observations and Pandora are solely due to spatial representation. In the case of this coincidence with its high degree of spatial and temporal variability, none of the simulated satellite products are capable of resolving this dominant subgrid scale feature observed by GeoTASO and Pandora, and without careful analysis the satellite products could appear to have a low bias if extrapolating validation datasets are extended to include column amounts that are likely representative of extreme subgrid features too large for the satellite retrieval to resolve.

Figure 9 illustrates that a linear relationship appears to degrade above some threshold value of NO₂ in these cases. Above the threshold, the more polluted NO₂ columns observed by Pandora are likely occurring over spatial scales smaller than the satellite resolutions, as shown in the preceding example. This theoretical threshold decreases as the spatial resolution is coarsened. The decreasing linear slope with increasing pixel size simply results from this flattening of the satellite-to-Pandora relationship at the higher NO₂ values. This threshold does not imply that the satellite cannot detect such large amounts of pollution, but it instead reflects that in these regions NO₂ enhancements of these large magnitudes are not sustained over spatial scales that are representative of current/future space-based retrievals. Such behavior makes sense if the high NO₂ values are associated with localized heterogeneous features rather than more mixed regional-scale enhancements, which is a reasonable conceptual model for urban areas such as these. The value of the threshold likely varies by region and may not be generalizable, but these results suggest that there is a limit to the magnitude of pollution that can be validated using the localized measurements of Pandora (i.e., Pandora is only representative of each satellite product up to a certain pollution scale). As longer-term Pandora data records become available, it is possible that examining temporal variance statistics at each site can allow for the development of screening criteria to help identify such situations.
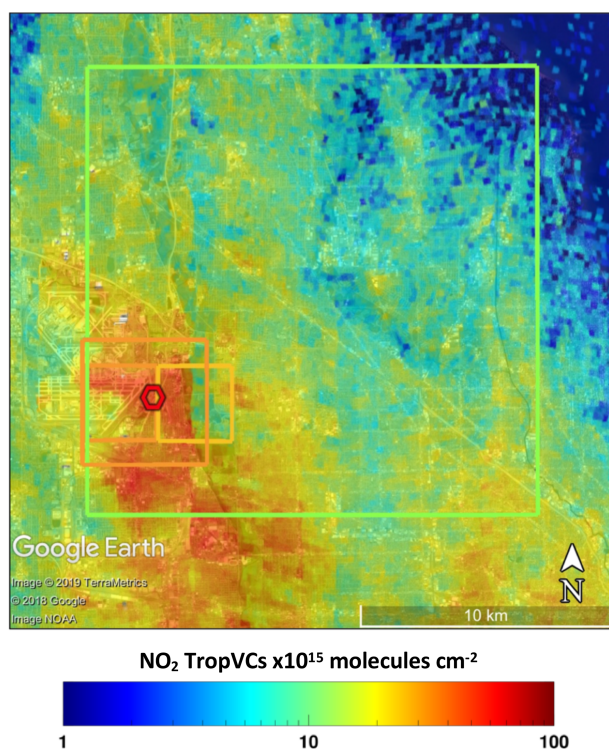
Figure 10. Map of GeoTASO TropVCs on a $\log_{10}$ color scale at the $250\,\mathrm{m} \times 250\,\mathrm{m}$ spatial resolution during the morning raster of 1 June 2017 over Schiller Park (same as Fig. 4) with the overlaid simulated pixels for TEMPO, TROPOMI, and OMI encompassing the Schiller Park ground site colored by the magnitude of their upscaled TropVC. The hexagon indicates the location of the Pandora spectrometer and is colored by the observed Pandora NO$_2$ TropVC. Base map created in © Google Earth Pro.

The data from these campaigns are not sufficient for confidently quantifying such thresholds but do allow the sensitivity to different thresholds to be explored by examining how the statistics vary as pollution thresholds for Pandora coincidences are decreased. To do this, each regression is repeated by excluding points for which Pandora TropVCs exceed 40×10^{15} molecules cm^{-2} (dashed regression line in Fig. 9) and exceed 20×10^{15} molecules cm^{-2} (solid black regression line in Fig. 9). Only the most polluted Schiller Park coincidence is excluded when filtering by Pandora TropVCs less than 40×10^{15} molecules cm^{-2}. The example discussed in association with Fig. 10 shows that this is a case in which Pandora and GeoTASO are observing a highly localized feature. With the removal of this point, the slopes increase (improve) and the correlations remain similar, with the exception of a notable improvement at OMI resolution. The TEMPO scale comparison resembles the results at the nominal spatial scale, but the slope still decreases as data are scaled to the coarser TROPOMI and OMI resolutions. When considering coincidences limited to Pandora TropVCs less than 20×10^{15} molecules cm^{-2}, the correlations all degrade by

5 %–10 % due to the smaller dynamic range with similar noise but are still on order of 0.8 or better. Pixel size has less influence on calculated slope, with only a 7 % decrease in slope between the nominal pixel size and the OMI scale resolutions. Even below these thresholds, individual coincidences are often associated with the influence of spatial heterogeneity as shown by the vertical whiskers. In fact, no single Pandora site was completely homogeneous for all coincidences (determined by the standard deviation of the GeoTASO measurements in the area surrounding each site as well as visual examination of Pandora time series near the times of coincidences). However, if this type of pollution environment is sampled enough, the variability could be statistically characterized sufficiently enough to allow the identification of retrieval biases or errors.

This analysis shows that, if a priori information at high enough spatial resolution is applied in the satellite retrieval, Pandora and satellite-scale products can compare well statistically within these regions up to the nadir pixel size of OMI for Pandora columns less than 20×10^{15} molecules cm^{-2} (although individual points can still deviate largely from the 1 : 1 relation due to subpixel variability). The threshold pollution scale for TROPOMI comparisons to Pandora is higher, somewhere between 20 and 40×10^{15} molecules cm^{-2}, and for TEMPO it is higher still, up to 40×10^{15} molecules cm^{-2}. This analysis would benefit from more coincidences in the range of 20–60×10^{15} molecules cm^{-2} to more confidently define pollution-scale thresholds acceptable for Pandora and satellite product comparisons. Acceptable pollution ranges for data comparison may even vary from region to region as each urban area could have distinct spatial variability patterns.

These results suggest that Pandora spectrometer direct-sun observations are very useful for validating satellite NO$_2$ products at the spatial resolutions of TEMPO and TROPOMI, as the products are highly correlated with points tightly spanning both sides of the 1 : 1 line for values of up to approximately 30×10^{15} molecules cm^{-2} (and perhaps higher, but this dataset lacks sufficient observations above that level). However, even at the finest satellite product resolution (TEMPO), comparisons with Pandora observations are not exempt from outliers caused by extreme degrees of subpixel heterogeneity. When choosing validation locations, areas known to have consistently strong spatiotemporal variability at spatial scales finer than the satellite retrieval (e.g., Schiller Park) should be avoided. When possible, additional measurements (i.e., high-resolution airborne mapping) would help investigate the uncertainty associated with spatial representativeness in the analysis of retrieval bias.

3.3 Comparison of OMI satellite products and ground-based Pandora measurements

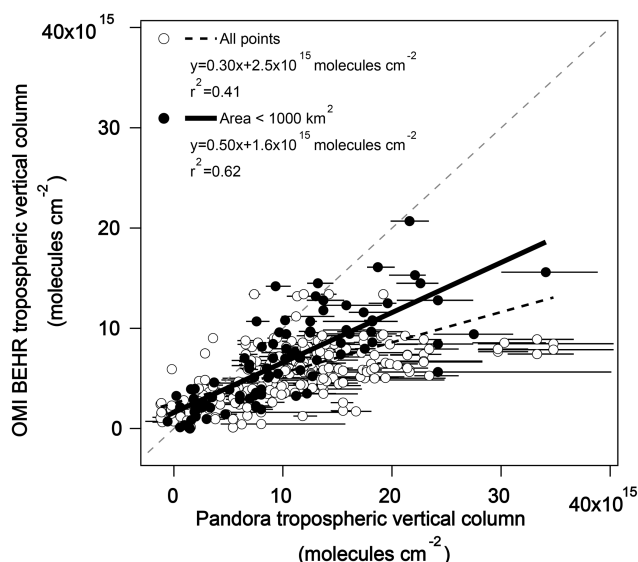During the LMOS and LA Basin flights, OMI was the highest-resolution space-based platform in orbit, as

Figure 11. OMI native pixel BEHR NO$_2$ tropospheric vertical column data vs. Pandora NO$_2$ tropospheric column. The filled circles indicate pixel areas less than $1000 \, \text{km}^2$. The linear fit to all points is shown in dashed black and the linear fit for pixels less than $1000 \, \text{km}^2$ is shown in solid black. Horizontal whiskers show the maximum and minimum of Pandora data $\pm 5 \, \text{min}$ of the OMI overpass. The thin dashed line is the 1 : 1 line.

TROPOMI was not launched until October of that year. Since 2004, OMI has been observing global NO$_2$ columns at a regional spatial scale on daily timescales. The simulated OMI comparisons in Sect. 3.2 are considered an idealized best-case scenario for data comparisons due to the near-nadir-spatial-resolution and the high-resolution a priori assumptions used for GeoTASO AMFs. In actuality, OMI's pixel area increases over 1200 % from nadir to the swath edge, and most of the a priori inputs to the AMF calculations have coarser spatial resolutions than those used in these GeoTASO retrievals. This section demonstrates how actual OMI observations compare with the Pandora measurements in the LMOS and LA Basin domains during May–July 2017 to cover the time period during which OMI BEHR data were available and the Pandora spectrometers were operating in the two regions.

Figure 11 shows the 444 coincidences between the OMI BEHR TropVC and the Pandora TropVC (Pandora total column minus the OMI stratospheric column) with the best-fit linear regression for all points shown as a dashed black line. The points are further subset by considering only pixel areas less than $1000 \, \text{km}^2$ (black points and solid black regression line). Coincidence and comparison criteria include OMI pixels unaffected by the row anomaly encompassing the location of a Pandora spectrometer with a MODIS cloud fraction less than 20 %. Pandora data are averaged within a $\pm 5 \, \text{min}$ window of the OMI overpass time to be consistent with the temporal window used to assess variability in Sect. 3.1.

Considering all pixel areas, the BEHR TropVCs are moderately correlated with Pandora TropVCs ($r^2 = 0.41$) with a low slope (0.30) and are on average biased 50 % lower than Pandora. Considering only pixels with areas less than $1000 \, \text{km}^2$, correlation and slope improve by at least 50 % ($r^2 = 0.62$, slope $= 0.5$), again demonstrating the sensitivity of these direct comparisons to the areal representativeness of the satellite pixel. Restricting OMI pixels to even smaller sizes (not shown) does not result in further statistical improvement, probably because the number of coincidences quickly decreases as the areal threshold decreases (40 coincidences when including only pixel areas below $500 \, \text{km}^2$ and 23 coincidences for below $400 \, \text{km}^2$). The slopes shown in Fig. 11 are notably lower than those calculated from the idealized GeoTASO-simulated idealized nadir OMI pixels discussed in Sect. 3.2, by 58 % for all size pixels and 30 % for pixel area $< 1000 \, \text{km}^2$. These differences are indicative of improvements associated with using higher spatial resolution a priori information, as used in the GeoTASO retrievals.

The horizontal whiskers in Fig. 11 show the maximum and minimum in the Pandora measurement within the 10 min temporal window of the OMI overpass. Some of these coincidences are impacted by very large variations in NO$_2$ measured by Pandora within a small window of the OMI overpass. This suggests that, in addition to the magnitude of NO$_2$ as a potential heterogeneity screen discussed in Sect. 3.2, coincidence criteria based on the temporal variability of the fast measurements from Pandora could also help identify coincidences that may be impacted by small-scale highly heterogeneous environments.

To further explore sensitivity to AMF, Table 4 lists the linear regression statistics of OMI retrievals against Pandora observations for three products: the BEHR vertical column data shown in Fig. 11, the NASA standard product V3 vertical column (SP TropVC), and tropospheric slant column products from OMI and Pandora (TropSC) (Recall that BEHR also uses the SP slant column). Consistently comparing these slant and vertical column statistics with respect to Pandora observations provides an assessment of the influence of AMF a priori assumptions. For these Pandora coincidences, SP TropVCs are on average 51 % lower than BEHR TropVCs, resulting in a 40 % lower slope for SP TropVCs and Pandora. These comparisons demonstrate improvement due to incorporating the higher-resolution a priori inputs in the BEHR product. Improvements to the spatial resolution of a priori input for OMI AMF calculations have previously been shown to help reduce biases (Russell et al., 2011; Lin et al., 2014). There is a minimal difference in r^2 when comparing Pandora to BEHR or SP TropVCs for OMI pixels less than $1000 \, \text{km}^2$. But there is a dramatic loss in correlation between SP TropVCs and Pandora as pixel size increases, demonstrating that the impact of coarse a priori input worsens with increasing pixel size.

OMI tropospheric slant column (TropSC) comparisons with Pandora are slightly better than SP vertical column (SP

Table 4. Statistics between Pandora and OMI BEHR and SP TropVC and TropSC based on OMI pixel area.

	Slope			Intercept ($\times 10^{15}$ molecules cm^{-2})			r^2			N
OMI pixel area	BEHR TropVC	SP TropVC	TropSC	BEHR TropVC	SP TropVC	TropSC	BEHR TropVC	SP TropVC	TropSC	
$< 1000\,\mathrm{km}^2$	0.50	0.34	0.44	1.6	1.2	1.3	0.62	0.61	0.65	125
All	0.30	0.18	0.26	2.5	1.9	2.4	0.41	0.32	0.39	444

TropVC) comparisons, indicating that the SP AMF is introducing additional variance in the SP TropVC product. The loss in skill associated with applying the SP AMF is evidenced by the 30 % decrease in the slope for all coincidences and 22 % decrease for pixels less than 1000 km² in comparison to TropSC comparisons. The application of the finer-resolution BEHR AMF largely retains the amount of skill in the TropSC with a slight improvement in slope.

Previous comparisons of OMI with Pandora direct-sun column measurements in urban environments have also shown low to moderate correlations for vertical-to-vertical column comparisons with low biases found in areas subject to spatial heterogeneity of NO₂ (Lamsal et al., 2014; Reed et al., 2015; Kim et al., 2016; Goldberg et al., 2017). Similar results have also been obtained from comparisons with ground-based MAX-DOAS retrievals (Lin et al., 2014; Chan et al., 2015). Monthly averaged OMI NASA SP V3 observations were also found to be biased low using Pandora observations in Korea (Herman et al., 2018) and MAX-DOAS observations in Hong Kong (Krotkov et al., 2017), but both studies found consistent seasonal trends in the satellite- and surface-based column measurements. Not all comparison studies result in such a strong low bias associated with OMI. Boersma et al. (2018) found no low bias in OMI observations, but care was taken to limit influence by spatial variability, and there were only 31 coincidences ranging from 5–10 × 10¹⁵ molecules cm⁻², which are pollution levels that are likely less influenced by extreme spatial heterogeneity. Lamsal et al. (2014) noted that MAX-DOAS/OMI bias (−16.3 %) was not quite as low as reported by these Pandora comparisons in a study in the polluted (up to 40 × 10¹⁵ molecules cm⁻²) Tsukuba region of Japan, which may be related to either the larger spatial footprint of MAX-DOAS observations (∼ 10 km from Boersma et al., 2018) or different spatiotemporal thresholds appropriate for that specific region. For validation purposes, there should be value in combining direct-sun and all-sky (MAX-DOAS) measurements at the same locations. The MAX-DOAS measurements, with their ability to measure omnidirectionally, can be more spatially representative albeit at the expense of coarser temporal resolution and higher measurement uncertainties, while the direct-sun observations are more frequent with very low measurement uncertainties but potentially larger influences of local-scale variability.

Theoretically, satellite retrieval uncertainty could be better quantified with measurements from airborne simulators like GeoTASO that are capable of mapping entire satellite pixels. During LMOS/LA Basin flights, GeoTASO sampled inside 177 OMI pixels within ±1 h of the OMI overpass. However, during these 2017 flights, no OMI pixels were entirely mapped within a ±1 h period from the OMI overpass; the maximum OMI pixel area covered was approximately 80 % in one coincidence and only 7 pixels were mapped by at least 50 %. Therefore, GeoTASO data from these campaigns do not provide enough data to independently assess OMI bias. However, with the finer spatial resolutions of new platforms (e.g., TROPOMI and TEMPO), mapping satellite pixels within an acceptable temporal threshold from the overpass time should be more easily achieved, allowing an additional point of view between the space-based observations and ground-based platforms such as Pandora.

4　Conclusions

During May–June 2017, an observing strategy was executed to build a number of airborne high-spatial-resolution gapless maps with GeoTASO over networks of ground-based instruments along the western shore of Lake Michigan and in the LA Basin. Each region had a network of five Pandora spectrometers (10 total) operating in direct-sun mode, providing accurate NO₂ vertical column measurements at high temporal resolution with which to compare GeoTASO NO₂ TropVC retrievals. The subkilometer airborne NO₂ retrievals from GeoTASO are highly correlated with Pandora spectrometer observations with a slope near 1 : 1. Most of the apparent discrepancies between GeoTASO and Pandora TropVCs are associated with high variability and are therefore sensitive to assumptions made for identifying coincidences: e.g., the unidirectional Pandora viewing footprint vs. the omnidirectional 750 m radius used to subset GeoTASO. At least one incidence was from a likely GeoTASO TropVC bias induced by inaccurate a priori assumptions in a complex environment that is difficult to simulate (a sea breeze frontal convergence zone). Future considerations for such comparisons should include assessments based on temporal and spatial criteria, as well as different environmental conditions. Despite these individual discrepancies, the GeoTASO

retrievals accurately capture the spatiotemporal variability of NO$_2$ in these regions.

The raster mapping strategy at subkilometer resolution allows assessment of the impacts of subpixel heterogeneity within the larger areal pixel resolutions of past, present, and planned satellite instruments. Data from each raster are binned to fixed grids to simulate the pixel areas of nadir observations from TEMPO (3 km × 3 km), TROPOMI (5 km × 5 km), and OMI (18 km × 18 km). Distinct spatial features (sea breeze front, industrial areas, etc.) within urban areas of Los Angeles and Chicago can be distinguished at TEMPO, and perhaps even TROPOMI, scale but cannot be resolved at the nadir area scale of OMI. The coarseness of the OMI scale can even alias the apparent spatial location of NO$_2$ maxima within urban regions. As pixel size increases, the linear statistics with Pandora degrade in these urban regions due to nonresolvable spatial heterogeneity that is most often associated with highly polluted features that lie within only a portion of the larger pixels. This suggests that for validation purposes, there may be a practical limit on the magnitude of Pandora measurements that can be compared to satellite retrievals as occurrences of exceptionally high concentration NO$_2$ features appear to occur at spatial scales smaller than the satellite resolutions. In the regions of this study, this resolvable pollution scale appears to be near 20×10^{15} molecules cm^{-2} at OMI spatial resolution. TROPOMI- and TEMPO-resolution satellite products have the capability to compare well with Pandora at higher pollution scales, although more coincidences above 30×10^{15} molecules cm^{-2} would help refine this conclusion further. These thresholds provide only general guidance, as individual coincidences can still be influenced by spatial heterogeneity at any magnitude of pollution. However, if such environments are sampled enough, the variability could be statistically characterized sufficiently enough to allow the identification of retrieval biases or errors.

Actual OMI observations show poorer agreement with Pandora direct-sun observations than is indicated by the idealized simulated satellite product. This is partially attributable to the decrease in OMI spatial resolution off-nadir, with some of the coincidences having pixel areas up to 1200 % larger than the nadir pixel areas. When BEHR TropVC pixels are filtered to include only areas less than 1000 km^2, the Pandora linear regression slope improves by 66 % and r^2 by 51 %. The degraded real-world performance is also due to coarse information in the AMF calculation. An indication of this sensitivity is shown by the vertical column regression statistics against Pandora coincidences, in which the BEHR product has a better slope than the NASA standard product. Further, the regression of slant column products is better than the SP vertical column, showing that uncertainties introduced by coarse AMF assumptions can even degrade the satellite NO$_2$ products.

These results reiterate the past challenges in using OMI observations to evaluate the magnitude of NO$_2$ pollution within urban areas, as the large footprint spatially averages NO$_2$ over an area that in reality has more fine-scale features. With the launch of TROPOMI in October 2017 and the geostationary sensors arriving in the next decade, their unprecedented spatial and temporal resolutions offer significantly improved capability for accurately assessing pollution within urban areas. Future validation work of satellite retrievals should consider using networks collecting frequent direct-sun Pandora observations spread throughout a wide range of pollution environments that, through time, can collect enough data to statistically characterize effects of small-scale heterogeneity in order to evaluate satellite retrievals. Assessing temporal behavior of the Pandora observations (and the Geostationary observations when available) surrounding coincidence times can add additional information about whether or not any resultant difference between the measurements can be associated with spatiotemporal heterogeneity (e.g., the sea breeze front at LA Main Street in Figs. 6 and 7). Future small-scale campaigns similar to those reported here, combining high-spatial-resolution airborne mapping observations and high-temporal-resolution ground-based reference measurements with high-resolution modeling studies, provide a framework for the validation of geostationary air quality measurements that will greatly enhance their usage for science and applications.

Author contributions. LMJ processed the GeoTASO NO$_2$ retrievals and led the writing of the manuscript. All coauthors provided feedback on the methodology and contributed to the final manuscript. JAA, RBP, and LMJ led flight planning activities for LMOS and/or the LA Basin flights. SJJ, MGK, and LMJ collected the GeoTASO dataset during LMOS and/or the LA Basin flights, and SJJ and MGK calibrated and processed the L1b spectra for GeoTASO. RBP provided the NAM-CMAQ analysis used in the vertical column retrieval. JJS, LCV, and DW set up and monitored the Pandora spectrometers during LMOS. RS and NA provided the Pandora spectrometers for the LA Basin and NA set up the LA Basin Pandora instruments. AC, MM, and MT processed the Pandora NO$_2$ retrievals.

References

Beirle, S., Boersma, K. F., Platt, U., Lawrence, M. G., and Wagner, T.: Megacity Emissions and Lifetimes of Nitrogen Oxides Probed from Space, Science, 333, 1737–1739, https://doi.org/10.1126/science.1207824, 2011.

Boersma, K. F., Eskes, H. J., Dirksen, R. J., van der A, R. J., Veefkind, J. P., Stammes, P., Huijnen, V., Kleipool, Q. L., Sneep, M., Claas, J., Leitão, J., Richter, A., Zhou, Y., and Brunner, D.: An improved tropospheric NO$_2$ column retrieval algorithm for the Ozone Monitoring Instrument, Atmos. Meas. Tech., 4, 1905–1928, https://doi.org/10.5194/amt-4-1905-2011, 2011.

Boersma, K. F., Eskes, H. J., Richter, A., De Smedt, I., Lorente, A., Beirle, S., van Geffen, J. H. G. M., Zara, M., Peters, E., Van Roozendael, M., Wagner, T., Maasakkers, J. D., van der A, R. J., Nightingale, J., De Rudder, A., Irie, H., Pinardi, G., Lambert, J.-C., and Compernolle, S. C.: Improving algorithms and uncertainty estimates for satellite NO$_2$ retrievals: results from the quality assurance for the essential climate variables (QA4ECV) project, Atmos. Meas. Tech., 11, 6651–6678, https://doi.org/10.5194/amt-11-6651-2018, 2018.

Bourassa, A. E., McLinden, C. A., Sioris, C. E., Brohede, S., Bathgate, A. F., Llewellyn, E. J., and Degenstein, D. A.: Fast NO$_2$ retrievals from Odin-OSIRIS limb scatter measurements, Atmos. Meas. Tech., 4, 965–972, https://doi.org/10.5194/amt-4-965-2011, 2011.

Broccardo, S., Heue, K.-P., Walter, D., Meyer, C., Kokhanovsky, A., van der A, R., Piketh, S., Langerman, K., and Platt, U.: Intrapixel variability in satellite tropospheric NO$_2$ column densities derived from simultaneous space-borne and airborne observations over the South African Highveld, Atmos. Meas. Tech., 11, 2797–2819, https://doi.org/10.5194/amt-11-2797-2018, 2018.

Bucsela, E. J., Krotkov, N. A., Celarier, E. A., Lamsal, L. N., Swartz, W. H., Bhartia, P. K., Boersma, K. F., Veefkind, J. P.,

Gleason, J. F., and Pickering, K. E.: A new stratospheric and tropospheric NO$_2$ retrieval algorithm for nadir-viewing satellite instruments: applications to OMI, Atmos. Meas. Tech., 6, 2607–2626, https://doi.org/10.5194/amt-6-2607-2013, 2013.

Burrows, J. P., Weber, M., Buchwitz, M., Rozanov, V., Ladstätter-Weißenmayer, A., Richter, A., DeBeek, R., Hoogen, R., Bramstedt, K., and Eichmann, K.-U.: The global ozone monitoring experiment (GOME): Mission concept and first scientific results, J. Atmos. Sci., 56, 151–175, 1999.

Cede, A.: Manual for Blick Software Suite 1.3, version 7, available at: http://pandonia.net/media/documents/BlickSoftwareSuite_Manual_v7.pdf (last access: 26 March 2019), 2017.

CEOS: A Geostationary Satellite Constellation for Observing Global Air Quality: An International Path Forward, available at: http://ceos.org/document_management/Virtual_Constellations/ACC/Documents/AC-VC_Geostationary-Cx-for-Global-AQ-final_Apr2011.pdf (last access: 6 March 2018), 2011.

Chan, K. L., Hartl, A., Lam, Y. F., Xie, P. H., Liu, W. Q., Cheung, H. M., Lampel, J., Pöhler, D., Li, A., Xu, J., Zhou, H. J., Ning, Z., and Wenig, M. O.: Observations of tropospheric NO$_2$ using ground based MAX-DOAS and OMI measurements during the Shanghai World Expo 2010, Atmos. Environ., 119, 45–58, https://doi.org/10.1016/j.atmosenv.2015.08.041, 2015.

Chance, K. and Kurucz, R. L.: An improved high-resolution solar reference spectrum for earth's atmosphere measurements in the ultraviolet, visible, and near infrared, J. Quant. Spectrosc. Ra., 111, 1289–1295, https://doi.org/10.1016/j.jqsrt.2010.01.036, 2010.

EPA: Technical Note – Guidance for Developing Enhanced Monitoring Plans, available at: https://www3.epa.gov/ttnamti1/files/ambient/pams/PAMSEMPGuidance.pdf, last access: 1 April 2019a.

EPA: Air Quality Statistics Report, available at: https://www.epa.gov/outdoor-air-quality-data/air-quality-statistics-report, last access: 18 March 2019b.

Goldberg, D. L., Lamsal, L. N., Loughner, C. P., Swartz, W. H., Lu, Z., and Streets, D. G.: A high-resolution and observationally constrained OMI NO$_2$ satellite retrieval, Atmos. Chem. Phys., 17, 11403–11421, https://doi.org/10.5194/acp-17-11403-2017, 2017.

Hastings, D. and Dunbar, P.: Global Land One-kilometer Base Elevation (GLOBE) Digital Elevation Model, Documentation, Volume 1.0, National Oceanic and Atmospheric Administration, National Geophysical Data Center, Boulder, Colorado 80303, USA, 1999.

Heckel, A., Kim, S.-W., Frost, G. J., Richter, A., Trainer, M., and Burrows, J. P.: Influence of low spatial resolution a priori data on tropospheric NO$_2$ satellite retrievals, Atmos. Meas. Tech., 4, 1805–1820, https://doi.org/10.5194/amt-4-1805-2011, 2011.

Herman, J., Cede, A., Spinei, E., Mount, G., Tzortziou, M., and Abuhassan, N.: NO$_2$ column amounts from ground-based Pandora and MFDOAS spectrometers using the direct-sun DOAS technique: Intercomparisons and application to OMI validation, J. Geophys. Res., 114, D13307, https://doi.org/10.1029/2009JD011848, 2009.

Herman, J., Evans, R., Cede, A., Abuhassan, N., Petropavlovskikh, I., and McConville, G.: Comparison of ozone retrievals from the Pandora spectrometer system and Dobson spectrophotome-

ter in Boulder, Colorado, Atmos. Meas. Tech., 8, 3407–3418, https://doi.org/10.5194/amt-8-3407-2015, 2015.

Herman, J., Spinei, E., Fried, A., Kim, J., Kim, J., Kim, W., Cede, A., Abuhassan, N., and Segal-Rozenhaimer, M.: NO$_2$ and HCHO measurements in Korea from 2012 to 2016 from Pandora spectrometer instruments compared with OMI retrievals and with aircraft measurements during the KORUS-AQ campaign, Atmos. Meas. Tech., 11, 4583–4603, https://doi.org/10.5194/amt-11-4583-2018, 2018.

IGACO: International Global Atmospheric Chemistry Observations Strategy Theme Report, No. ESA SP-1282, GW No. 159, WMO TD No. 1235, available at: http://www.fao.org/gtos/igos/docs/IGACO-Theme-Report-2004-4.pdf (last access: 6 March 2018), 2004.

Ingmann, P., Veihelmann, B., Langen, J., Lamarre, D., Stark, H., and Courrèges-Lacoste, G. B.: Requirements for the GMES Atmosphere Service and ESA's implementation concept: Sentinels-4/-5 and -5p, Remote Sens. Environ., 120, 58–69, https://doi.org/10.1016/j.rse.2012.01.023, 2012.

Janz, S., Judd L., and Kowalewski, M.: Lake Michigan Ozone Study GeoTASO NO$_2$ Vertical Columns, NASA ASDC Lake Michigan Ozone Study Repository, available at: https://www-air.larc.nasa.gov/missions/lmos/index.html, last access: 4 November 2019.

Judd, L. M., Al-Saadi, J. A., Valin, L. C., Pierce, R. B., Yang, K., Janz, S. J., Kowalewski, M. G., Szykman, J. J., Tiefengraber, M., and Mueller, M.: The Dawn of Geostationary Air Quality Monitoring: Case Studies From Seoul and Los Angeles, Front. Environ. Sci., 6, 85, https://doi.org/10.3389/fenvs.2018.00085, 2018.

Kim, H. C., Lee, P., Judd, L., Pan, L., and Lefer, B.: OMI NO$_2$ column densities over North American urban cities: the effect of satellite footprint resolution, Geosci. Model Dev., 9, 1111–1123, https://doi.org/10.5194/gmd-9-1111-2016, 2016.

Kim, J., Kim, M., and Choi, M.: Monitoring Aerosol Properties in East Asia from Geostationary Orbit: GOCI, MI and GEMS, in: Air Pollution in Eastern Asia: An Integrated Perspective, Springer, Cham, 323–333, 2017.

Kleipool, Q. L., Dobber, M. R., de Haan, J. F., and Levelt, P. F.: Earth surface reflectance climatology from 3 years of OMI data, J. Geophys. Res., 113, D18308, https://doi.org/10.1029/2008JD010290, 2008.

Kowalewski, M. G. and Janz, S. J.: Remote sensing capabilities of the GEO-CAPE airborne simulator, Proc. SPIE 9218, Earth Observing Systems XIX, 17–21 August 2014, San Diego, California, USA, 92181I, https://doi.org/10.1117/12.2062058, 2014.

Krotkov, N. A., Lamsal, L. N., Celarier, E. A., Swartz, W. H., Marchenko, S. V., Bucsela, E. J., Chan, K. L., Wenig, M., and Zara, M.: The version 3 OMI NO$_2$ standard product, Atmos. Meas. Tech., 10, 3133–3149, https://doi.org/10.5194/amt-10-3133-2017, 2017.

Lamsal, L. N., Krotkov, N. A., Celarier, E. A., Swartz, W. H., Pickering, K. E., Bucsela, E. J., Gleason, J. F., Martin, R. V., Philip, S., Irie, H., Cede, A., Herman, J., Weinheimer, A., Szykman, J. J., and Knepp, T. N.: Evaluation of OMI operational standard NO$_2$ column retrievals using in situ and surface-based NO$_2$ observations, Atmos. Chem. Phys., 14, 11587–11609, https://doi.org/10.5194/acp-14-11587-2014, 2014.

Lamsal, L. N., Janz, S. J., Krotkov, N. A., Pickering, K. E., Spurr, R. J. D., Kowalewski, M. G., Loughner, C. P., Crawford, J. H., Swartz, W. H., and Herman, J. R.: High-

resolution NO$_2$ observations from the Airborne Compact Atmospheric Mapper: Retrieval and validation: High-Resolution NO$_2$ Observations, J. Geophys. Res.-Atmos., 122, 1953–1970, https://doi.org/10.1002/2016JD025483, 2017.

Laughner, J. L., Zhu, Q., and Cohen, R. C.: The Berkeley High Resolution Tropospheric NO$_2$ product, Earth Syst. Sci. Data, 10, 2069–2095, https://doi.org/10.5194/essd-10-2069-2018, 2018a.

Laughner, J., Zhu, Q., and Cohen, R.: Berkeley High Resolution (BEHR) OMI NO$_2$ – Native pixels, monthly profiles, UC Berkeley Dash, Dataset, https://doi.org/10.6078/D1N086, 2018b.

Laughner, J. L., Zhu, Q., and Cohen, R. C.: Evaluation of version 3.0B of the BEHR OMI NO$_2$ product, Atmos. Meas. Tech., 12, 129–146, https://doi.org/10.5194/amt-12-129-2019, 2019.

Lawrence, J. P., Anand, J. S., Vande Hey, J. D., White, J., Leigh, R. R., Monks, P. S., and Leigh, R. J.: High-resolution measurements from the airborne Atmospheric Nitrogen Dioxide Imager (ANDI), Atmos. Meas. Tech., 8, 4735–4754, https://doi.org/10.5194/amt-8-4735-2015, 2015.

Leitch, J. W., Delker, T., Good, W., Ruppert, L., Murcray, F., Chance, K., Liu, X., Nowlan, C., Janz, S. J., Krotkov, N. A., Pickering, K. E., Kowalewski, M., and Wang, J.: The GeoTASO airborne spectrometer project, Earth Observing Systems XIX, 17–21 August 2014, San Diego, California, United States, Proc. SPIE, 9218, 92181H-9, https://doi.org/10.1117/12.2063763, 2014.

Levelt, P. F., Oord, G. H. J. van den, Dobber, M. R., Malkki, A., Visser, H., Vries, J. de, Stammes, P., Lundell, J. O. V., and Saari, H.: The ozone monitoring instrument, IEEE T. Geosci. Remote, 44, 1093–1101, https://doi.org/10.1109/TGRS.2006.872333, 2006.

Li, J., Chen, S., Qin, W., Murefu, M., Wang, Y., Yu, Y., and Zhen, Z.: ANALYSIS OF ACCURACY OF MODIS BRDF PRODUCT (MCD43 C6) BASED ON MISR LAND SURFACE BRF PRODUCT – A CASE STUDY OF THE CENTRAL PART OF NORTHEAST ASIA, Int. Arch. Photogramm. Remote Sens. Spatial Inf. Sci., XLII-3, 819–823, https://doi.org/10.5194/isprs-archives-XLII-3-819-2018, 2018.

Liang, J., Horowitz, L. W., Jacob, D. J., Wang, Y., Fiore, A. M., Logan, J. A., Gardner, G. M., and Munger, J. W.: Seasonal budgets of reactive nitrogen species and ozone over the United States, and export fluxes to the global atmosphere, J. Geophys. Res., 103, 13435–13450, https://doi.org/10.1029/97JD03126, 1998.

Lin, J.-T., Martin, R. V., Boersma, K. F., Sneep, M., Stammes, P., Spurr, R., Wang, P., Van Roozendael, M., Clémer, K., and Irie, H.: Retrieving tropospheric nitrogen dioxide from the Ozone Monitoring Instrument: effects of aerosols, surface reflectance anisotropy, and vertical profile of nitrogen dioxide, Atmos. Chem. Phys., 14, 1441–1461, https://doi.org/10.5194/acp-14-1441-2014, 2014.

Liu, F., Beirle, S., Zhang, Q., Dörner, S., He, K., and Wagner, T.: NO$_x$ lifetimes and emissions of cities and power plants in polluted background estimated by satellite observations, Atmos. Chem. Phys., 16, 5283–5298, https://doi.org/10.5194/acp-16-5283-2016, 2016.

Liu, X., Bhartia, P. K., Chance, K., Spurr, R. J. D., and Kurosu, T. P.: Ozone profile retrievals from the Ozone Monitoring Instrument, Atmos. Chem. Phys., 10, 2521–2537, https://doi.org/10.5194/acp-10-2521-2010, 2010.

Lucht, W., Schaaf, C. B., and Strahler, A. H.: An algorithm for the retrieval of albedo from space using semiempirical BRDF models, IEEE T. Geosci. Remote, 38, 977–998, https://doi.org/10.1109/36.841980, 2000.

LuftBlick: Pandora Direct Sun Total NO$_2$ Vertical Columns, Pandonia Global Network, http://judd2019.pandonia-global-network.org/ (last access: 4 November 2019), 2017.

McLinden, C. A., Olsen, S. C., Hannegan, B., Wild, O., Prather, M. J., and Sundet, J.: Stratospheric ozone in 3-D models: A simple chemistry and the cross-tropopause flux, J. Geophys. Res., 105, 14653–14665, https://doi.org/10.1029/2000JD900124, 2000.

Meier, A. C., Schönhardt, A., Bösch, T., Richter, A., Seyler, A., Ruhtz, T., Constantin, D.-E., Shaiganfar, R., Wagner, T., Merlaud, A., Van Roozendael, M., Belegante, L., Nicolae, D., Georgescu, L., and Burrows, J. P.: High-resolution airborne imaging DOAS measurements of NO$_2$ above Bucharest during AROMAT, Atmos. Meas. Tech., 10, 1831–1857, https://doi.org/10.5194/amt-10-1831-2017, 2017.

Noguchi, K., Richter, A., Rozanov, V., Rozanov, A., Burrows, J. P., Irie, H., and Kita, K.: Effect of surface BRDF of various land cover types on geostationary observations of tropospheric NO$_2$, Atmos. Meas. Tech., 7, 3497–3508, https://doi.org/10.5194/amt-7-3497-2014, 2014.

Nowlan, C. R., Liu, X., Leitch, J. W., Chance, K., González Abad, G., Liu, C., Zoogman, P., Cole, J., Delker, T., Good, W., Murcray, F., Ruppert, L., Soo, D., Follette-Cook, M. B., Janz, S. J., Kowalewski, M. G., Loughner, C. P., Pickering, K. E., Herman, J. R., Beaver, M. R., Long, R. W., Szykman, J. J., Judd, L. M., Kelley, P., Luke, W. T., Ren, X., and Al-Saadi, J. A.: Nitrogen dioxide observations from the Geostationary Trace gas and Aerosol Sensor Optimization (GeoTASO) airborne instrument: Retrieval algorithm and measurements during DISCOVER-AQ Texas 2013, Atmos. Meas. Tech., 9, 2647–2668, https://doi.org/10.5194/amt-9-2647-2016, 2016.

Nowlan, C. R., Liu, X., Janz, S. J., Kowalewski, M. G., Chance, K., Follette-Cook, M. B., Fried, A., González Abad, G., Herman, J. R., Judd, L. M., Kwon, H.-A., Loughner, C. P., Pickering, K. E., Richter, D., Spinei, E., Walega, J., Weibring, P., and Weinheimer, A. J.: Nitrogen dioxide and formaldehyde measurements from the GEOstationary Coastal and Air Pollution Events (GEO-CAPE) Airborne Simulator over Houston, Texas, Atmos. Meas. Tech., 11, 5941–5964, https://doi.org/10.5194/amt-11-5941-2018, 2018.

Palmer, P. I., Jacob, D. J., Chance, K., Martin, R. V., Spurr, R. J. D., Kurosu, T. P., Bey, I., Yantosca, R., Fiore, A., and Li, Q.: Air mass factor formulation for spectroscopic measurements from satellites: Application to formaldehyde retrievals from the Global Ozone Monitoring Experiment, J. Geophys. Res., 106, 14539–14550, https://doi.org/10.1029/2000JD900772, 2001.

Pierce, R. B., Schaack, T., Al-Saadi, J. A., Fairlie, T. D., Kittaka, C., Lingenfelser, G., Natarajan, M., Olson, J., Soja, A., Zapotocny, T., Lenzen, A., Stobie, J., Johnson, D., Avery, M. A., Sachse, G. W., Thompson, A., Cohen, R., Dibb, J. E., Crawford, J., Rault, D., Martin, R., Szykman, J., and Fishman, J.: Impacts of background ozone production on Houston and Dallas, Texas, air quality during the Second Texas Air Quality Study field mission, J. Geophys. Res., 114, D00F09, https://doi.org/10.1029/2008JD011337, 2009.

Popp, C., Brunner, D., Damm, A., Van Roozendael, M., Fayt, C., and Buchmann, B.: High-resolution NO$_2$ remote sensing from the Airborne Prism EXperiment (APEX) imaging spectrometer, Atmos. Meas. Tech., 5, 2211–2225, https://doi.org/10.5194/amt-5-2211-2012, 2012.

Prather, M.: Catastrophic loss of stratospheric ozone in dense volcanic clouds, J. Geophys. Res., 97, 10187–10191, https://doi.org/10.1029/92JD00845, 1992.

Reed, A. J., Thompson, A. M., Kollonige, D. E., Martins, D. K., Tzortziou, M. A., Herman, J. R., Berkoff, T. A., Abuhassan, N. K., and Cede, A.: Effects of local meteorology and aerosols on ozone and nitrogen dioxide retrievals from OMI and pandora spectrometers in Maryland, USA during DISCOVER-AQ 2011, J. Atmos. Chem., 72, 455–482, https://doi.org/10.1007/s10874-013-9254-9, 2015.

Rothman, L. S., Gordon, I. E., Barbe, A., Benner, D. C., Bernath, P. F., Birk, M., Boudon, V., Brown, L. R., Campargue, A., Champion, J.-P., Chance, K., Coudert, L. H., Dana, V., Devi, V. M., Fally, S., Flaud, J.-M., Gamache, R. R., Goldman, A., Jacquemart, D., Kleiner, I., Lacome, N., Lafferty, W. J., Mandin, J.-Y., Massie, S. T., Mikhailenko, S. N., Miller, C. E., Moazzen-Ahmadi, N., Naumenko, O. V., Nikitin, A. V., Orphal, J., Perevalov, V. I., Perrin, A., Predoi-Cross, A., Rinsland, C. P., Rotger, M., Šimečková, M., Smith, M. A. H., Sung, K., Tashkun, S. A., Tennyson, J., Toth, R. A., Vandaele, A. C., and Vander Auwera, J.: The HITRAN 2008 molecular spectroscopic database, J. Quant. Spectrosc. Ra., 110, 533–572, https://doi.org/10.1016/j.jqsrt.2009.02.013, 2009.

Russell, A. R., Perring, A. E., Valin, L. C., Bucsela, E. J., Browne, E. C., Wooldridge, P. J., and Cohen, R. C.: A high spatial resolution retrieval of NO$_2$ column densities from OMI: method and evaluation, Atmos. Chem. Phys., 11, 8543–8554, https://doi.org/10.5194/acp-11-8543-2011, 2011.

Schaaf, C. and Wang, Z.: MCD43A1 MODIS/Terra+Aqua BRDF/Albedo Model Parameters Daily L3 Global – 500m V006, NASA EOSDIS Land Processes DAAC, https://doi.org/10.5067/modis/mcd43a1.006, 2015.

Schönhardt, A., Altube, P., Gerilowski, K., Krautwurst, S., Hartmann, J., Meier, A. C., Richter, A., and Burrows, J. P.: A wide field-of-view imaging DOAS instrument for two-dimensional trace gas mapping from aircraft, Atmos. Meas. Tech., 8, 5113–5131, https://doi.org/10.5194/amt-8-5113-2015, 2015.

Souri, A. H., Choi, Y., Pan, S., Curci, G., Nowlan, C. R., Janz, S. J., Kowalewski, M. G., Liu, J., Herman, J. R., and Weinheimer, A. J.: First Top-Down Estimates of Anthropogenic NO$_x$ Emissions Using High-Resolution Airborne Remote Sensing Observations, J. Geophys. Res.-Atmos., 123, 3269–3284, https://doi.org/10.1002/2017JD028009, 2018.

Spurr, R. J. D.: VLIDORT: A linearized pseudo-spherical vector discrete ordinate radiative transfer code for forward model and retrieval studies in multilayer multiple scattering media, J. Quant. Spectrosc. Ra., 102, 316–342, https://doi.org/10.1016/j.jqsrt.2006.05.005, 2006.

Stajner, I., Davidson, P., Byun, D., McQueen, J., Draxler, R., Dickerson, P., and Meagher, J.: US National Air Quality Forecast Capability: Expanding Coverage to Include Particulate Matter, in: Air Pollution Modeling and its Application XXI, edited by: Steyn, D. G. and Trini Castelli, S., Springer Netherlands, 379–384, 2011.

Tack, F., Merlaud, A., Iordache, M.-D., Danckaert, T., Yu, H., Fayt, C., Meuleman, K., Deutsch, F., Fierens, F., and Van Roozendael, M.: High-resolution mapping of the NO$_2$ spatial distribution over Belgian urban areas based on airborne APEX remote sensing, Atmos. Meas. Tech., 10, 1665–1688, https://doi.org/10.5194/amt-10-1665-2017, 2017.

Tack, F., Merlaud, A., Meier, A. C., Vlemmix, T., Ruhtz, T., Iordache, M.-D., Ge, X., van der Wal, L., Schuettemeyer, D., Ardelean, M., Calcan, A., Constantin, D., Schönhardt, A., Meuleman, K., Richter, A., and Van Roozendael, M.: Intercomparison of four airborne imaging DOAS systems for tropospheric NO$_2$ mapping – the AROMAPEX campaign, Atmos. Meas. Tech., 12, 211–236, https://doi.org/10.5194/amt-12-211-2019, 2019.

Thalman, R. and Volkamer, R.: Temperature dependent absorption cross-sections of O$_2$–O$_2$ collision pairs between 340 and 630 nm and at atmospherically relevant pressure, Phys. Chem. Chem. Phys., 15, 15371, https://doi.org/10.1039/c3cp50968k, 2013.

van Geffen, J. H. G., Eskes, H. J., Boersma, K. F., Maasakkers, J. D., and Veefkind, J. P.: TROPOMI ATBD of the total and tropospheric NO$_2$ data products, KNMI, available at: https://sentinel.esa.int/documents/247904/2476257/Sentinel-5P-TROPOMI-ATBD-NO2-data-products, last access: 16 April 2019.

Valin, L. C., Russell, A. R., Bucsela, E. J., Veefkind, J. P., and Cohen, R. C.: Observation of slant column NO$_2$ using the superzoom mode of AURA-OMI, Atmos. Meas. Tech., 4, 1929–1935, https://doi.org/10.5194/amt-4-1929-2011, 2011a.

Valin, L. C., Russell, A. R., Hudman, R. C., and Cohen, R. C.: Effects of model resolution on the interpretation of satellite NO$_2$ observations, Atmos. Chem. Phys., 11, 11647–11655, https://doi.org/10.5194/acp-11-11647-2011, 2011b.

Vandaele, A. C., Hermans, C., Simon, P. C., Carleer, M., Colin, R., Fally, S., Mérienne, M. F., Jenouvrier, A., and Coquart, B.: Measurements of the NO$_2$ absorption cross-section from $42\,000\,cm^{-1}$ to $10\,000\,cm^{-1}$ (238–1000 nm) at 220 K and 294 K, J. Quant. Spectrosc. Ra., 59, 171–184, https://doi.org/10.1016/S0022-4073(97)00168-4, 1998.

Volkamer, R., Spietz, P., Burrows, J., and Platt, U.: High-resolution absorption cross-section of glyoxal in the UV–vis and IR spectral ranges, J. Photoch. Photobio. A, 172, 35–46, https://doi.org/10.1016/j.jphotochem.2004.11.011, 2005.

Zoogman, P., Liu, X., Suleiman, R. M., Pennington, W. F., Flittner, D. E., Al-Saadi, J. A., Hilton, B. B., Nicks, D. K., Newchurch, M. J., Carr, J. L., Janz, S. J., Andraschko, M. R., Arola, A., Baker, B. D., Canova, B. P., Chan Miller, C., Cohen, R. C., Davis, J. E., Dussault, M. E., Edwards, D. P., Fishman, J., Ghulam, A., González Abad, G., Grutter, M., Herman, J. R., Houck, J., Jacob, D. J., Joiner, J., Kerridge, B. J., Kim, J., Krotkov, N. A., Lamsal, L., Li, C., Lindfors, A., Martin, R. V., McElroy, C. T., McLinden, C., Natraj, V., Neil, D. O., Nowlan, C. R., O'Sullivan, E. J., Palmer, P. I., Pierce, R. B., Pippin, M. R., Saiz-Lopez, A., Spurr, R. J. D., Szykman, J. J., Torres, O., Veefkind, J. P., Veihelmann, B., Wang, H., Wang, J., and Chance, K.: Tropospheric emissions: Monitoring of pollution (TEMPO), J. Quant. Spectrosc. Ra., 186, 17–39, https://doi.org/10.1016/j.jqsrt.2016.05.008, 2017.